Sep 13, 2022

Structural basis for $Na_V1.7$ inhibition by pore blockers

Jiangtao Zhang[1,2*], Yiqiang Shi[3*], Zhuo Huang[3*], Yue Li[4,5], Bei Yang[4], Jianke Gong[2], Daohua Jiang[1,5**]

[1] Laboratory of Soft Matter Physics, Institute of Physics, Chinese Academy of Sciences, Beijing 100190, China

[2] College of Life Science and Technology, Key Laboratory of Molecular Biophysics of MOE, Huazhong University of Science and Technology, Wuhan, Hubei, China

[3] State Key Laboratory of Natural and Biomimetic Drugs, Department of Molecular and Cellular Pharmacology, School of Pharmaceutical Sciences, Peking University Health Science Center, Beijing, 100191, China

[4] National Laboratory of Biomacromolecules, CAS Center for Excellence in Biomacromolecules, Institute of Biophysics, Chinese Academy of Sciences, Beijing 100101, China

[5] University of Chinese Academy of Sciences, Beijing 100049, China

* These authors contribute equally to this project.

** Correspondence emails: jiangdh@iphy.ac.cn (D.J.)

Abstract

Voltage-gated sodium channel $Na_V1.7$ plays essential roles in pain and odour perception. $Na_V1.7$ variants cause pain disorders. Accordingly, $Na_V1.7$ has elicited extensive attention in developing new analgesics. Here we present cryo-EM structures of human $Na_V1.7$/β1/β2 complexed with inhibitors XEN907, TC-N1752 and $Na_V1.7$-IN2, elucidating specific binding sites and modulation mechanism for the pore-blockers. These inhibitors bind in the central cavity blocking ion permeation, but engage different parts of the cavity wall. XEN907 directly causes α- to π-helix transition of DIV-S6 helix, which tightens the fast inactivation gate. TC-N1752 induces π-helix transition of DII-S6 helix mediated by a conserved asparagine on DIII-S6, which closes the activation gate. $Na_V1.7$-IN2 serves as a pore blocker without causing conformational change. Electrophysiological results demonstrate that XEN907 and TC-N1752 stabilize $Na_V1.7$ in inactivated state and delay the recovery from inactivation. Our results provide structural framework for $Na_V1.7$ modulation by pore-blockers, and important implications for developing subtype-selective analgesics.

Introduction

Voltage-gated sodium (Na_V) channels play fundamental roles in generating and propagating action potentials in excitable cells[1,2]. In humans, nine highly related Na_V channel isoforms ($Na_V1.1$-1.9) are expressed with specific tissue patterns[3]. Among them, $Na_V1.7$, encoded by *SCN9A*, is highly expressed in peripheral sensory neurons such as nociceptive and sympathetic neurons[4], as well as in brain subcortical regions including the thalamus, medial amygdala and the axons of olfactory epithelium[5,6]. Gain-of-function mutations of $Na_V1.7$ are linked to pain disorders such as erythromelalgia, paroxysmal extreme pain disorder, small fiber neuropathy and painful diabetic neuropathy[7-11]. Strikingly, loss-of-function mutations in $Na_V1.7$ were reported to cause congenital insensitivity to pain and anosmia[12-15]. The growing evidence clearly demonstrates that $Na_V1.7$ mediates the transmission of pain signals to the brain[16,17]. Consequently, $Na_V1.7$ represents a new target for developing potentially non-addictive analgesics. Extensive efforts have been made in searching for $Na_V1.7$ selective inhibitors by many programs, several candidate drugs have been undergoing clinical trials such as Funapide (TV-45070, XEN402), Vixotrigine (BIIB074), and PF-05089771 [18-20]. However, most of them failed due to the lack of selectivity or weak efficacy[21,22]. Therefore, understanding the structural discriminations among Na_V isoforms and the mechanism underlying the functional role of $Na_V1.7$ in pain perception are critical to overcome current barriers.

Recent structural advances in mammalian Na_V channels revealed the subunits assembly, activation and fast inactivation, gating mechanism, and modulation by natural toxins and synthetic antiarrhythmic drugs[23-30]. The Na_V channel structures manifest highly conserved key structural elements such as voltage-sensor domain (VSD), central cavity and fast inactivation gate. However, the conserved N-terminus domain (NTD), which is essential for Na_V channel functions[31-34], its structure and how it regulates Na_V channels remain unknown. Despite the high structural similarity, several aryl sulfonamide

antagonists were reported to potently and selectively inhibit $Na_V1.7$ or $Na_V1.3$ by binding to the VSD_{IV}[35,36], retaining potential in finding Na_V channel subtype-selective inhibitors. XEN907, a spirooxindole derivative closely related to Funapide (XEN402), showed potent inhibition of $Na_V1.7$ at nanomolar concentration[37]. TC-N1752, a state-dependent $Na_V1.7$ inhibitor, displayed analgesic efficacy in the formalin pain model[38]. $Na_V1.7$-inhibitor2 ($Na_V1.7$-IN2), an aryl carboxamide derivative developed as $Na_V1.7$ inhibitor for pain treatment by Amgen Inc[39]. The detailed binding sites for these specifically developed $Na_V1.7$ inhibitors and the molecular mechanisms underlying their modulation on $Na_V1.7$ remain elusive.

In this study, we describe the structural basis for the modulation of human $Na_V1.7$ by the three chemically different blockers. Our structures reveal that the large central cavity of $Na_V1.7$ accommodates multiple drug binding sites. The pore-blocking inhibitors also induce local conformational rearrangements of the pore-lining S6 helices, thus alter the channel gating property. Our results provide mechanistic insights into the inhibition of $Na_V1.7$ by small-molecule inhibitors, which should facilitate future structure-based drug design.

Results

Functional analysis of $Na_V1.7$ and structure of the NTD

The electrophysiological characteristics of human wide-type (WT) $Na_V1.7$ were validated by whole-cell voltage-clamp recording of the $Na_V1.7$ transient transfected HEK293T cells. $Na_V1.7$ generates rapid inward currents and quickly becomes inactivated in response to depolarizing pulses, yielding $V_{1/2}$ values for the voltage-dependence of activation and steady-state fast inactivation at −20.7 ± 0.7 mV (n=13) and −76.6 ± 0.9 mV (n=14) (Extended Data Fig. 1a), respectively, which are consistent with previous report[40]. In order to define the detailed binding sites for the antagonists, we purified

human WT $Na_V1.7/\beta1/\beta2$ complex sample in the presence of each antagonist individually (Extended Data Fig. 1b and c), and performed cryo-electron microcopy (cryo-EM) single-particle analysis of the purified channel complexes. The final reconstruction maps of the $Na_V1.7/\beta1/\beta2$ complexed with XEN907 (designated as $Na_V1.7^{XEN}$), TC-N1752 (designated as $Na_V1.7^{TCN}$) and Na1.7-IN2 (designated as $Na_V1.7^{IN2}$) were refined to 3.2, 3.1 and 3.1 Å, respectively (Extended Data Fig. 2). The high-quality density map allowed us to build accurate models for the protein and the antagonists (Extended Data Figs. 3 and 4). The overall structure of the pore-forming α-subunit and the binding poses of β1 and β2 to the α-subunit resemble previously reported Na_V structures[23,25,30] (Extended Data Fig. 4a and b).

Interestingly, the density for the NTD of the $Na_V1.7^{XEN}$ map is surprisingly better than the other two structures or the reported mammalian Na_V structures[23-25,30], presumably because the map reconstruction of $Na_V1.7^{XEN}$ has better particle angular distribution than the other two maps (Extended Data Figs. 2b-d, 5a). With the assistance of AlphaFold2 model, a reliable NTD model was built for the $Na_V1.7$ based on the EM density (Fig. 1a, Extended Data Fig. 5a-d). The NTD model (P7-R30 and P49-S113) is composed of two helices and two anti-parallel β sheets with loops connecting them (Fig. 1b, Extended Data Fig. 5d). The loop connecting domain I S2 helix ($S2_I$) and $S3_I$, which interacts with the loop between the NTD β2 sheet and $S0_I$, agrees well with the density of our $Na_V1.7^{XEN}$ map (Fig. 1c). However, it shows marked difference with previously reported $Na_V1.7$ structure containing the E406K mutation[30] (Fig. 1c). The model differences are probably because the density for this region was not well-resolved in the previous EM maps of Na_V channels. The NTD is located under the VSD_I and forms extensive interactions with the VSD_I. The $S0_I$ appears to be very hydrophobic, which closely engages the NTD via conserved hydrophobic interactions (Fig. 1d, Extended Data Fig. 5e). In addition, R116 on the $S0_I$ forms polar interactions with the main-chain carbonyl oxygen atoms of N101 and T103 (Fig. 1d). Deletion of the NTD of $Na_V1.5$ was reported

to abolish the sodium current[31], our structural observations suggest that removal of the NTD could cause destabilization of the VSD_I which is known to be important for the Na_V channels activation[41]. In line with this hypothesis, the dominant-negative effect (DNE) variant R121W of cardiac sodium channel $Na_V1.5$ (equivalent to R116 in $Na_V1.7$), which causes Brugada Syndrome (BrS), drastically reduces the peak current to undetectable level[31,33]. We also mapped twelve disease-associated mutations of Na_V channels on the NTD of $Na_V1.7$ (Fig. 1b, Extended Data Fig. 5e), revealing the critical role of the NTD for Na_V channel functions. For instance, R99 plays a critical role in stabilizing the hydrophobic core of the NTD, and its long side-chain forms electrostatic interactions with D77 and D79 at distances of 3.3 Å and 3.9 Å, respectively. The R99 also forms cation-π interaction with Y92 at a distance of 3.1 Å. (Fig. 1b). The pathogenic mutations of R99W, R99H, D79G and Y82C were reported as loss-of-function variants, which may abolish these specific interactions and cause incorrect protein folding or reduced plasma membrane localization[31,32,34,42].

$Na_V1.7$ modulation by XEN907

We found XEN907 preferentially inhibits $Na_V1.7$ in inactivated-state. When holding the $Na_V1.7$-expressing HEK239T cells at −120 mV to maintain the channels in resting-state, applying of 100 nM XEN907 only decreases peak current of $Na_V1.7$ by ~30% after 10 repetitive pulses to reach the steady-state inhibition; in contrast, 100 nM XEN907 drops peak current of $Na_V1.7$ over 80% when cells were held at −80 mV to drive the channel into inactivated-state (Extended Data Fig. 6a and b). The dose-dependent response curves show that the inactivated-state inhibition (IC_{50}=4.5 ± 1.3 nM, n=4-7) of XEN907 is over 1000-fold more potent than that of the resting-state inhibition (IC_{50}=4.7 ± 2.9 μM, n=4-5) (Fig. 2a).

The cryo-EM structure of $Na_V1.7^{XEN}$ revealed one XEN907 molecule bound in the central cavity (Fig. 2b-d, Extended Data Fig. 6e and f), which is located underneath the

selectivity filter (SF) closing to $S6_{IV}$ helix (Fig. 2c). The pentyl tail points to the D_{III}-D_{IV} fenestration (Fig. 2c and d); the benzodioxole lies in the middle of the cavity interacting with Q360, F391 and I394 (Fig. 2c); and the spirooxindole core is sandwiched by S1697 and F1748/V1752 (Fig. 2c). Importantly, the spirooxindole group of XEN907 also interacts with K1406 of the sodium selectivity determining DEKA locus[43], preventing the exit of Na^+ from the SF (Fig. 2c). Compared to the reported $Na_V1.7$ structure[30] (denoted as $Na_V1.7^{apo}$), one helical turn on $S6_{IV}$ of $Na_V1.7^{XEN}$ underwent α- to π-helix transition upon XEN907 binding through direct interaction with V1752 (Fig. 2e, Extended Data Fig. 6g, Supplementary Video 1). Similar helical transitions on the pore-lining S6 helices were observed in $Ca_V1.1$-diltiazem and $Ca_V3.1$-Z944 structures[44,45], indicating that the S6 helix is a prominent target for pore-blockers to modulate channel function. In addition, XEN907 interacts with F1748 on $S6_{IV}$ at a distance of 3.2 Å, the critical residue for local anesthetic or antiarrhythmic (LA) drugs binding[25,26,29,46], suggesting that XEN907 partially occupies the binding site of LA drugs. However, no π-helix transition was observed upon LA drugs binding[25,26,47]. Superposition of the $Na_V1.7^{XEN}$ with the $Na_V1.7^{apo}$ showed no obvious shift for the overall position of the $S6_{IV}$ helix, but all residues after V1752 on $S6_{IV}$ of $Na_V1.7^{XEN}$ underwent a spiral rotation of one-third helical turn (Fig. 2e, Extended Data Fig. 6g). Consequently, the D_I-D_{IV} fenestration is closed (Fig. 2d), and the intracellular activation gate of $Na_V1.7^{XEN}$ is slightly smaller than that of the $Na_V1.7^{apo}$ as L1760 displacing I1759 (Fig. 2f, Extended Data Fig. 4c). Intriguingly, we noticed that the fast inactivation gate of $Na_V1.7^{XEN}$ became more hydrophobic as M1754 displacing the hydrophilic N1753, and the ‘fast inactivation particle’ Ile1742-Phe1743-Met1744 (IFM) motif slightly shifts upward (Fig. 2g). We therefore postulate that the XEN907 induced π-helix transition enhances the binding of IFM-motif to the hydrophobic receptor site, which further stabilizes the channel in the inactivated state. To validate this hypothesis, we assessed the changes of voltage-dependent fast inactivation and recovery from fast inactivation upon XEN907 binding. Although XEN907 does not affect the voltage

dependence of activation, the antagonist dramatically shifts the voltage-dependent fast inactivation to more hyperpolarized potential in a concentration-dependent manner (~11 mV with 100 nM XEN907) (Fig. 2h, Extended Data Fig. 6c and d). In addition, the recovery rate from fast inactivation was significantly slowed by over 3-fold upon XEN907 binding (Fig. 2i). To further verify the effect of XEN907 on delaying the fast inactivation, we sought to see if a N1753M mutation can delay the recovery from fast inactivation in the absence of XEN907, and a M1754N mutation can abolish the delay of recovery from fast inactivation in the presence of XEN907. Unfortunately, no currents can be evoked from either of the two mutants (Extended Data Fig. 6h). Nevertheless, these results confirmed that the XEN907 binding indeed stabilizes $Na_V1.7$ in the inactivated state. Our $Na_V1.7^{XEN}$ structure demonstrates that XEN907 not only blocks the ion conductance by binding in the central cavity, but also causes the α- to π-helix transition on $S6_{IV}$ helix which tightens the fast inactivation gate to prevent gate opening.

$Na_V1.7$ modulation by TC-N1752

We next examined the inhibitory effect of TC-N1752 on $Na_V1.7$. Similar to XEN907, TC-N1752 potently inhibits $Na_V1.7$ in the inactivated-state (Extended Data Fig. 7a and b). TC-N1752 displayed weak inhibition on $Na_V1.7$ when holding at −120 mV (Fig. 3a, Extended Data Fig. 7b). By contrast, the antagonist exhibited strong inhibition of $Na_V1.7$ when holding at −80 mV (Fig. 3a, Extended Data Fig. 7b). The dose-dependent response curve yields IC_{50} value of 199.5 ± 33.5 nM (n=3-8) for TC-N1752 using the inactivated-state protocol, whereas 10 μM TC-N1752 only reduces ~30% of the peak current using the resting-state protocol (Fig. 3a). Meanwhile, we tested the potency of TC-N1752 in inhibiting human $Na_V1.5$, the results showed that TC-N1752 can also potently inhibit $Na_V1.5$ similar to $Na_V1.7$ (Extended Data Fig. 7c-e), suggesting that TC-N1752 is a non-selective blocker for Na_V channels.

In our 3.1 Å resolution cryo-EM map of $Na_V1.7^{TCN}$, a piece of unambiguous L-shaped density was observed inside the central cavity, which fits TC-N1752 molecule perfectly (Extended Data Fig. 7g and h). The TC-N1752 occupies large space of the central cavity and physically blocks the ion path (Fig. 3b-d). The antagonist is stabilized by multiple polar and non-polar interactions mainly from $S6_I$, $S6_{III}$ and $S6_{IV}$ helices (Fig. 3c and e). The trifluoromethoxy-phenyl group forms π-π stacking with the F1748 of the LA site and blocks the D_{III}-D_{IV} fenestration (Fig. 3c and d); the piperidinyl ring is located right under the SF at a distance of ~5 Å; Q360 from D_I P-loop engages both the piperidinyl ring and the triazine ring by polar interactions with distances of 3.9 Å; a hydrogen-bond between the conserved N395 on $S6_I$ and the triazine ring reinforces the TC-N1752 binding; and the conserved N1450 on $S6_{III}$ forms another hydrogen-bond with the acetamide group further strengthening the binding (Fig. 3c). F391, L398, L964, L1449 and Y1755 also contribute to stabilize TC-N1752 through hydrophobic and van de Waals interactions. Accordingly, TC-N1752 induces marked local conformational rearrangements of the pore-lining S6 helices through these extensive interactions (Fig. 3e-g). Strikingly, despite little direct interaction with TC-N1752 was observed, $S6_{II}$ helix underwent an α- to π-helix transition at the position of ~7 Å away from the phenyl ring of TC-N1752 (Fig. 3e and f, Extended Data Fig. 7i, Supplementary Video 2). A closer look at the binding site revealed that the π-helix transition of the $S6_{II}$ helix is mediated by the conserved N1450 on $S6_{III}$ (Fig. 3e). TC-N1752 shifts and rotates the side-chains of L1449 and N1450 toward the antagonist. The rotated N1450 forces F963 on $S6_{II}$ helix shifted upward about one-third helical turn, eventually one turn of π-helix was formed when the rotation reached G955 (Fig. 3e). In contrast to the XEN907 induced π-helix transition without overall helix shift (Fig. 2e), TC-N1752 indirectly caused π-helix transition shifts the $S6_{II}$ toward the activation gate axis up to 5 Å at the cytoplasmic end (Fig. 3f). The shift of the $S6_{II}$ helix not only shuts the D_I-D_{II} fenestration (Fig. 3d), but also closes the intracellular activation gate, which is almost completely sealed by the

constriction residues of A402, L968, I1457 and I1759 from $S6_I$, $S6_{II}$, $S6_{III}$ and $S6_{IV}$, respectively (Fig. 2g, Supplementary Video 2). The resulting activation gate of $Na_V1.7^{TCN}$ is significantly smaller than the gate of $Na_V1.7^{XEN}$, $Na_V1.7^{IN2}$ and the reported mammalian Na_V structures[23-25,30] (Extended Data Fig. 4c). These structural observations suggest that the $Na_V1.7^{TCN}$ structure may represent a drug-induced new inactivated-state distinct from previous reports. Meanwhile, our electrophysiological data showed that the voltage-dependent fast inactivation of $Na_V1.7$ were dramatically shifted to hyperpolarized potential by ~14 mV in the presence of 10 μM TC-N1752 (Fig. 3h), supporting the structural observation that TC-N1752 binding stabilizes the channel in the inactivated-state. However, no effect on the voltage dependence of activation was observed with 10 μM TC-N1752 (Extended Data Fig. 7f). In addition, the recovery rate from fast inactivation were only slightly delayed in the presence of 10 μM TC-N1752 (Fig. 3i), which is in agreement with the nearly identical fast inactivation gate between the $Na_V1.7^{TCN}$ and $Na_V1.7^{apo}$. Collectively, our $Na_V1.7^{TCN}$ structure elucidated that TC-N1752 can potently inhibit $Na_V1.7$ by physical pore-blocking, and also alter the channel gating property via inducing structural rearrangements of the pore-lining S6 helices.

$Na_V1.7$ inhibition by $Na_V1.7$-IN2

Distinct from the state-dependent inhibition of $Na_V1.7$ by XEN907 and TC-N1752, $Na_V1.7$-IN2 exhibits potent inhibition of $Na_V1.7$ in both resting-state (holding at −120 mV; IC_{50}=12.6 ± 5.4 nM, n=4-6) and inactivated-state (holding at −80 mV; IC_{50}=10.2 ± 4.4 nM, n=4-8) with almost the same affinity (Fig. 4a, Extended Data Fig. 8a and b). In addition, $Na_V1.7$-IN2 displayed potent inhibition of human $Na_V1.5$ with an IC_{50} value of 13.6 ± 5.6 nM (n=4-8) (Extended Data Fig. 8c-e), suggesting that $Na_V1.7$-IN2 is also a non-selective blocker.

The EM map of $Na_V1.7^{IN2}$ revealed a strong U-shaped density for one $Na_V1.7$-IN2 molecule lying in the middle of the central cavity (Fig. 4b-d, Extended Data Fig. 8g and

h). The $Na_V1.7$-IN2 was stabilized in the cavity primarily by interactions from the P-loops and S6 helices. The fluoro-methylphenoxy group interacts with Q360, F391 and I394; the pyrimidine ring wedges between S1697 and F1748; and the benzamide engages F1405 (Fig. 4c). Notably, the carbonyl of the benzamide group closes to the K1406 of the SF at 4.2 Å (Fig. 4c). The $Na_V1.7$-IN2 reclines in the cavity parallel to the membrane plane to perfectly block the ion permeation (Fig. 4d). Compared to the XEN907 and TC-N1752, $Na_V1.7$-IN2 interacts loosely with the cavity wall of $Na_V1.7$. Consequently, the EM density of $Na_V1.7$-IN2 is slightly weaker than that of XEN907 and TC-N1752. And importantly, compared to the $Na_V1.7^{apo}$, no obvious conformational change of the $Na_V1.7^{IN2}$ structure was observed upon $Na_V1.7$-IN2 binding. The S6 helices and the activation gate is nearly identical as the $Na_V1.7^{apo}$ (Fig. 4e). In agreement with the structural observation, our electrophysiological data showed that $Na_V1.7$-IN2 causes negligible effect on either the voltage-dependent activation, fast inactivation or recovery from fast inactivation (Fig. 4f, Extended Data Fig. 8f). These results suggest that $Na_V1.7$-IN2 may serve as a pure pore-blocker, the fenestrations could be the main access for the antagonist to block the channel (Fig. 4d).

Weak selectivity for binding sites in the central cavity

Site-2 neurotoxins, local anesthetic and anti-arrhythmic drugs are known to bind in the central cavity of Na_V channels to modulate Na_V channel functions with little subtype selectivity[48,49]. Cryo-EM structures of the cardiac sodium channel $Na_V1.5$ bound anti-arrhythmic drugs Flecainide, Quinidine and Propafenone revealed that the canonical LA site is located in the central cavity close to the conserved F1762 on the $S6_{IV}$ helix[25,26,29]. The site-2 neurotoxin binding site was recently disclosed from the cryo-EM structure of human $Na_V1.3$-Bulleyaconitine A complex, which is also located in the central cavity but distinct from the canonical LA-drug site[50]. Superposition of the LA-drug bound $Na_V1.5$ structures with our antagonist bound $Na_V1.7$ structures revealed that the binding sites share common key interactions (Fig. 5a-c). All of the six pore-blockers interact with the

conserved Phe of the LA site on $S6_{IV}$, meanwhile, five blockers interact with the Q360-F391-I394 cluster from PM_I except Flecainide (Fig. 5d-f, Extended Data Fig. 9). These observations suggest that the LA site and the Q360-F392-I394 cluster are the hot-spots for pore-blockers binding to the Na_V channels. However, sequence alignment of pore helices of the nine Na_V isoforms illustrates that the LA site and Q360-F391 of the cluster are identical, I394 of the cluster is highly conserved with a Val substitution in some isoforms (Extended Data Fig. 9). Furthermore, we labelled all residues interacting with the six blockers within 5 Å, which are all highly conserved (Extended Data Fig. 9). These observations demonstrate that the binding sites in the central cavity of the nine Na_V channels are indistinguishable, elucidating the difficulty in developing isoform-selective candidate drugs targeting the central cavity. To achieve the subtype selectivity for potential drugs targeting the pore, the accessibility, use- and state-dependent properties of the candidate drugs should be verified.

Discussion

Chronic pain is an extremely common disease that affects ~20% people of general population. Given the shortage of effective and non-addictive analgesics, new anti-pain drugs are eagerly awaited. Sodium channel $Na_V1.7$ plays an essential role in the transmission of pain signals to the brain[12,16,17], thus represents an attractive target for anti-pain therapeutics. However, $Na_V1.7$ is a very challenging target for developing selective candidate drugs, partially owing to the high sequence similarity within the nine Na_V isoforms. In this study, we presented cryo-EM structures of human $Na_V1.7$ in complexes with three pore-blocking antagonists. All three antagonists directly block the ion path. Strikingly, the binding of XEN907 and TC-N1752 also induces substantial local conformational changes in the pore-lining S6 helices that further alter the channel gating. Structural comparison between our antagonist bound $Na_V1.7$ and the anti-arrhythmic drugs bound $Na_V1.5$ structures revealed the hot-spots for drug binding inside the central

cavity. In addition, these common binding sites are strictly conserved among Na_V isoforms, making the central cavity almost impossible for binding isoform-selective drugs. However, there are also significant differences between the antagonists reported here and the previously reported LA drugs. The three pore-blockers are more potent in inhibiting $Na_V1.7$ with a factor of >100-fold than that of LA-drugs. In addition, no obvious conformational change of the pore-lining S6 helix was observed upon Flecainide, Quinidine or Propafenone binding, whereas XEN907 and TC-N1752 induce the α- to π-helix transition of $S6_{IV}$ and $S6_{II}$, respectively. The structural observations and the electrophysiological data suggest that XEN907 and TC-N1752 stabilize $Na_V1.7$ in the inactivated-state, while $Na_V1.7$-IN2 acts as a pure pore-blocker without altering channel gating. The use- and state-dependent inhibition of local anesthetic and anti-arrhythmic drugs are important for the drugs to preferentially block Na_V channels in favorable states[48,51], conferring a type of functional selectivity of the drugs despite binding to the non-selective receptor sites. Optimization of the potent and state-dependent antagonists XEN907 and TC-N1752 could possibly generate better potential analgesics targeting $Na_V1.7$. On the other hand, future effort on searching for $Na_V1.7$ selective inhibitors should focus on the relative variable regions of the Na_V isoforms, such as the VSDs. Taken together, our structures provide detailed mechanistic insights into the pore-blocking and modulation of $Na_V1.7$ by three antagonists, and we hope that our results provided implications that could facilitate the development of new analgesics for pain treatment.

Acknowledgements

We thank X. Huang, B. Zhu, X. Li, L. Chen, and other staff members at the Center for Biological Imaging (CBI), Core Facilities for Protein Science at the Institute of Biophysics, Chinese Academy of Science (IBP, CAS), and D. Sun at the SM10 Cryo-EM Facility at the Institute of Physics, Chinese Academy of Sciences (IOP, CAS) for the

support in cryo-EM data collection. We thank Prof. Xuejun Cai Zhang and Prof. Yan Zhao for their helpful discussions, Xiaoli Cui, Yanli Dong, Zhuoya Yu, Yan Wu and Wei Fan for their research assistant service. This work is funded by Institute of Physics, Chinese Academy of Sciences (E0VK101and E2V4101 to D.J.), the National Natural Science Foundation of China (32271272 to D.J., 31871083 and 82271498 to Z.H., 82071851 to J.G.), the Chinese Academy of Sciences Strategic Priority Research Program (31871083 and 81371432 to Z.H.), and the Chinese National Programs for Brain Science and Brain-like intelligence technology (2021ZD0202102 to Z.H.), and the program for HUST Academic Frontier Youth Team (5001170068 to J.G.).

Contributions

D.J. designed the experiments. J.Z. and Y.L. and B.Y. prepared sample for cryo-EM study and made all the constructs. J.Z. and D.J. collected cryo-EM data. D.J. processed the data, built and refined the models. J.Z. and Y.S. prepared figures. Y.S. and Z.H. collected the electrophysiology data. J.G., Z.H., and D.J. analyzed and interpreted the results. J.Z., Y.S. and D.J. wrote the paper, and all authors reviewed and revised the paper.

Competing interests

All authors declare no competing interests.

Table 1. Cryo-EM data collection, refinement and validation statistics

	$Na_V1.7$/β1/β2-XEN (EMD-33292) (PDB: 7XM9)	$Na_V1.7$/β1/β2-TCN (EMDB-33295) (PDB: 7XMF)	$Na_V1.7$/β1/β2-IN2 (EMDB-33296) (PDB: 7XMG)
Data collection and processing			
Magnification	105,000 ×	105,000 ×	105,000 ×
Voltage (kV)	300	300	300
Electron exposure (e^{-}/Å^2)	60	60	600
Defocus range (μm)	−1.2 ~ −2.2	−1.2 ~ −2.2	−1.2 ~ −2.2
Pixel size (Å)	1.04	1.04	1.04

Symmetry imposed	C1	C1	C1
Initial particle images (no.)	1,217,568	1,216,370	1,849,983
Final particle images (no.)	213,507	158,142	206,251
Map resolution (Å)	3.22	3.09	3.07
FSC threshold	0.143	0.143	0.143
Map resolution range (Å)	3.0 ~ 5.0	3.0 ~ 5.0	3.0 ~ 5.0
Refinement			
Initial model used (PDB code)	6J8J, AlphaFold2	$Na_V1.7$/β1/β2-XEN	$Na_V1.7$/β1/β2-XEN
Model resolution (Å)	3.39	3.40	3.20
FSC threshold	0.5	0.5	0.5
Map sharpening *B* factor (Å^2)	-115.4	-86.5	-111.0
Model composition			
Non-hydrogen atoms	12,472	11,772	11,762
Protein residues	1,523	1,433	1,431
Ligands	12	12	12
B factors (Å^2)			
Protein	87.2	70.1	71.8
Ligand	105.6	89.4	88.5
R.m.s. deviations			
Bond lengths (Å)	0.003	0.005	0.004
Bond angles (°)	0.604	0.700	0.741
Validation			
MolProbity score	2.41	2.62	2.87
Clashscore	10.0	11.6	13.9
Ramachandran plot			
Favored (%)	94.70	93.60	92.32
Allowed (%)	5.17	6.26	7.54
Disallowed (%)	0.13	0.14	0.14

Figure Legends

Figure 1. The NTD structure of $Na_V1.7$

a, The NTD structure located under the VSD_I of $Na_V1.7^{XEN}$. Superposition of $Na_V1.7^{XEN}$ and $Na_V1.7^{apo}$ (PDB code: 6j8j, colored in wheat). $Na_V1.7^{XEN}$ is shown in cartoon colored in blue (NTD), cyan (D_I), light red (D_{II}), light green (D_{III}), pink (D_{III}-D_{IV} linker) and light blue (D_{IV}), respectively. The same color scheme is used throughout the manuscript unless specified. The β subunits were omitted for clarity. **b**, The structure of the NTD. The locations of twelve disease-related mutations shown side chains in sticks. Loss- and gain-of-function mutations are highlighted in red and green, respectively. **c**, EM density for the loop between $S2_I$ and $S3_I$ of $Na_V1.7^{XEN}$. Residues with good density are shown side chains in sticks. **d**, Interactions

between $S0_I$ and the NTD. The side chains of key interacting residues are shown in sticks. Red dashed lines represent hydrogen bonds.

Figure 2. Structural basis for $Na_V1.7$ modulation by XEN907

a, The chemical structure and state-dependent inhibition of XEN907. Dose-dependent response curve of XEN907 holding at -120 mV (blue) and -80 mV (red), respectively. Data are mean +/- s.e.m. The n values of tested concentrations of 0.01 nM, 0.1 nM, 1 nM, 10 nM, 100 nM for holding at -80 mV are 5, 7, 4, 5, 5; the n values of tested concentrations of 1 nM, 10 nM, 100 nM, 1 μM, 10 μM for holding at -120 mV are 4, 5, 4, 4, 4, respectively. **b**, XEN907 binding site in $Na_V1.7$. The black dashed square indicates the area displayed in panel (**c**). The β subunits were omitted for clarity. **c**, Detailed binding site for XEN907. The side chains of key residues and XEN907 are shown in sticks. **d**, Cut-open sliced top-down view of $Na_V1.7$ pore module. XEN907 is depicted in spheres. **e**, XEN907 binding induces α- to π-helix transition in $S6_{IV}$. Compared to $Na_V1.7^{apo}$ (PDB code: 6j8j, colored in white), one helical turn of π-helix (colored in red) was formed upon XEN907 binding. Pink arrows indicate residue rotations. **f**, Gate comparison of $Na_V1.7^{XEN}$ and $Na_V1.7^{apo}$. **g**, Fast inactivation gate comparison of $Na_V1.7^{XEN}$ and $Na_V1.7^{apo}$. **h**, The effect of 100 nM XEN907 on the voltage-dependence of fast inactivation. Data are mean +/- s.e.m. The n values for control (black) and XEN907 (red) are 9 and 12 respectively. **i**, XEN907 binding slows recovery from fast inactivation. Data are mean +/- s.e.m. The n values for control (black) and XEN907 (red) are 12 and 9 respectively. Source data are provided.

Figure 3. Structural basis for $Na_V1.7$ modulation by TC-N1752

a, The chemical structure and state-dependent inhibition of TC-N1752. Dose-dependent response curve of TC-N1752 holding at -120 mV (blue) and -80 mV (red), respectively. Data are mean +/- s.e.m. The n values of tested concentrations of 0.01 μM, 0.03 μM, 0.1 μM, 0.3 μM, 1 μM, 10 μM for holding at -80 mV are 6, 8, 8, 5, 5, 3; and for holding at -120 mV are 6, 4, 4, 4, 5, 6, respectively. **b**, TC-N1752 binding site in $Na_V1.7$. The black dashed square indicates the area displayed in panel (**c**). The β subunits were omitted for clarity. **c**, Detailed binding site for TC-N1752. The side chains of key residues and TC-N1752 are shown in sticks. Red dashed lines represent polar interactions. **d**, Cut-open sliced top-down view of $Na_V1.7$ pore module. TC-N1752 is depicted in spheres. **e**, N1450 mediates the α- to π-helix transition of $S6_{II}$. Compared to $Na_V1.7^{apo}$ (PDB code: 6j8j, colored in white), a π- helix turn of Gly_{955}-Asn_{961} (colored in blue) was formed upon TC-N1752 binding. Pink arrows indicate the residue rotations. **f**, The $S6_{II}$ underwent conformational shift upon TC-N1752 binding compared to $Na_V1.7^{apo}$. **g**, Gate comparison of the $Na_V1.7^{TCN}$ and $Na_V1.7^{apo}$. Leu968 shifts toward the gate center and seals the gate. **h**, TC-N1752 shifts the voltage-dependence of fast inactivation

toward hyperpolarized potential. Data are mean +/- s.e.m. The n values for control (black) and TC-N1752 (red) are 10 and 8 respectively. **i**, The effect of 10 μM TC-N1752 on the recovery from fast inactivation. Data are mean +/- s.e.m. of n=5-10. The n values for control (black) and TC-N1752 (red) are 10 and 5 respectively. Source data are provided.

Figure 4. Structural basis for pore-blocking of $Na_V1.7$ by $Na_V1.7$-IN2

a, The chemical structure and state-independent inhibition of $Na_V1.7$-IN2. Dose-dependent response curve of $Na_V1.7$-IN2 holding at -120 mV (blue) and -80 mV (red), respectively. Data are mean +/- s.e.m. The n values of tested concentrations of 0.01 nM, 0.1 nM, 1 nM, 10 nM, 100 nM, 1 μM for holding at -80 mV are 4, 6, 6, 8, 6, 4; and for holding at -120 mV are 4, 4, 6, 4, 4, 5, respectively. **b**, $Na_V1.7$-IN2 binding site in $Na_V1.7$. The complex structure is shown in side view with $Na_V1.7$-IN2 depicted in spheres. The black dashed square indicates the area to be displayed in panels (**c**). The β subunits were omitted for clarity. **c**, Detailed binding site for $Na_V1.7$-IN2. The side chains of key residues and $Na_V1.7$-IN2 are shown in sticks. Red dashed line represents polar interaction. **d**, Cut-open sliced top-down view of $Na_V1.7$ pore module. $Na_V1.7$-IN2 is depicted in spheres. **e**, Gate comparison between $Na_V1.7^{IN2}$ and $Na_V1.7^{apo}$. Key residues at the gate constriction site shown side chains in sticks. **f**, The effect of 100 nM $Na_V1.7$-IN2 on the voltage-dependence of activation and fast inactivation. Data are mean +/- s.e.m. The n values for control (black) activation and inactivation are 10 and 8 respectively. The n values for TC-N1752 (red) are 7. Source data are provided.

Figure 5. Drug binding sites in the central cavity of Na_V channels

a-c, Superposition of the inhibitors bound in the central cavity of Na_V channel viewed from side (**a**), top-down (**b**), and bottom (**c**). XEN907, TC-N1752, $Na_V1.7$-IN2, Quinidine, Propafenone and Flecainide are shown in sticks and colored in gold, blue, pink, green, brown and purple, respectively. The surface of the binding spot of LA site for F1748 (green) and the Q360(purple)-F391(cyan)-I394(brown) cluster are highlighted. **d-f**, Close-up views of the drug binding site from panel (**a-c**). Side chains of the F1748 and the Q360-F391-I394 cluster are shown in sticks.

References

1 Catterall, W. A., Wisedchaisri, G. & Zheng, N. The chemical basis for electrical signaling. *Nat. Chem. Biol.* **13**, 455-463 (2017).

2 Hille, B. Ionic channels in excitable membranes. 3rd Edn (OUP USA, 2001).

3 Catterall, W. A., Goldin, A. L. & Waxman, S. G. Nomenclature and structure-function relationships of voltage-gated sodium channels. *Pharmacol. Rev.* **57**, 397-409 (2005).

4 Toledo-Aral, J. J. *et al.* Identification of PN1, a predominant voltage-dependent sodium channel expressed principally in peripheral neurons. *Proc. Natl. Acad. Sci. U S A* **94**, 1527-1532 (1997).

5 Kanellopoulos, A. H. *et al.* Mapping protein interactions of sodium channel $Na_V1.7$ using epitope-tagged gene-targeted mice. *EMBO J.* **37**, 427-445 (2018).

6 Branco, T. *et al.* Near-Perfect Synaptic Integration by Nav1.7 in Hypothalamic Neurons Regulates Body Weight. *Cell* **165**, 1749-1761 (2016).

7 Yang, Y. *et al.* Mutations in SCN9A, encoding a sodium channel alpha subunit, in patients with primary erythermalgia. *J. Med. Genet.* **41**, 171-174 (2004).

8 Dib-Hajj, S. D. *et al.* Gain-of-function mutation in Nav1.7 in familial erythromelalgia induces bursting of sensory neurons. *Brain* **128**, 1847-1854 (2005).

9 Fertleman, C. R. *et al.* SCN9A mutations in paroxysmal extreme pain disorder: allelic variants underlie distinct channel defects and phenotypes. *Neuron* **52**, 767-774 (2006).

10 Faber, C. G. *et al.* Gain of function $Na_V1.7$ mutations in idiopathic small fiber neuropathy. *Ann. Neurol.* **71**, 26-39 (2012).

11 Blesneac, I. *et al.* Rare $Na_V1.7$ variants associated with painful diabetic peripheral neuropathy. *Pain* **159**, 469-480 (2018).

12 Cox, J. J. *et al.* An SCN9A channelopathy causes congenital inability to experience pain. *Nature* **444**, 894-898 (2006).

13 Nilsen, K. B. *et al.* Two novel SCN9A mutations causing insensitivity to pain. *Pain* **143**, 155-158 (2009).

14 Cox, J. J. *et al.* Congenital insensitivity to pain: novel SCN9A missense and in-frame deletion mutations. *Hum. Mutat.* **31**, E1670-1686 (2010).

15 Weiss, J. *et al.* Loss-of-function mutations in sodium channel Nav1.7 cause anosmia. *Nature* **472**, 186-190 (2011).

16 Bennett, D. L., Clark, A. J., Huang, J., Waxman, S. G. & Dib-Hajj, S. D. The Role of Voltage-Gated Sodium Channels in Pain Signaling. *Physiol. Rev.* **99**, 1079-1151 (2019).

17 Dib-Hajj, S. D. & Waxman, S. G. Sodium Channels in Human Pain Disorders: Genetics and Pharmacogenomics. *Annu. Rev. Neurosci.* **42**, 87-106 (2019).

18 Alsaloum, M., Higerd, G. P., Effraim, P. R. & Waxman, S. G. Status of peripheral sodium channel blockers for non-addictive pain treatment. *Nat. Rev. Neurol.* **16**, 689-705 (2020).

19 Zakrzewska, J. M. *et al.* Safety and efficacy of a Nav1.7 selective sodium channel blocker in patients with trigeminal neuralgia: a double-blind, placebo-

controlled, randomised withdrawal phase 2a trial. *Lancet Neurol.* **16**, 291-300 (2017).

20 Cao, L. *et al.* Pharmacological reversal of a pain phenotype in iPSC-derived sensory neurons and patients with inherited erythromelalgia. *Sci. Transl. Med.* **8**, 335ra356 (2016).

21 Kingwell, K. Nav1.7 withholds its pain potential. *Nat. Rev. Drug Discov.* (2019).

22 Deuis, J. R. *et al.* Analgesic Effects of GpTx-1, PF-04856264 and CNV1014802 in a Mouse Model of NaV1.7-Mediated Pain. *Toxins (Basel)* **8** (2016).

23 Pan, X. *et al.* Structure of the human voltage-gated sodium channel Nav1.4 in complex with β1. *Science* **362** (2018).

24 Pan, X. *et al.* Molecular basis for pore blockade of human Na^+ channel Nav1.2 by the μ-conotoxin KIIIA. *Science* **363**, 1309-1313 (2019).

25 Jiang, D. *et al.* Structure of the Cardiac Sodium Channel. *Cell* **180**, 122-134.e110 (2020).

26 Jiang, D. *et al.* Open-state structure and pore gating mechanism of the cardiac sodium channel. *Cell* **184** (2021).

27 Clairfeuille, T. *et al.* Structural basis of α-scorpion toxin action on Nav channels. *Science* **363** (2019).

28 Jiang, D. *et al.* Structural basis for voltage-sensor trapping of the cardiac sodium channel by a deathstalker scorpion toxin. *Nat. Commun.* **12**, 128 (2021).

29 Li, Z. *et al.* Structural Basis for Pore Blockade of the Human Cardiac Sodium Channel Nav1.5 by the Antiarrhythmic Drug Quinidine. *Angew. Chem. Int. Ed. Engl.* **60** (2021).

30 Shen, H., Liu, D., Wu, K., Lei, J. & Yan, N. Structures of human Nav1.7 channel in complex with auxiliary subunits and animal toxins. *Science* **363**, 1303-1308 (2019).

31 Clatot, J. *et al.* Dominant-negative effect of SCN5A N-terminal mutations through the interaction of Nav1.5 α-subunits. *Cardiovasc. Res.* **96**, 53-63 (2012).

32 Wang, Z. *et al.* Calmodulin binds to the N-terminal domain of the cardiac sodium channel $Na_V1.5$. *Channels (Austin)* **14**, 268-286 (2020).

33 Holst, A. G. *et al.* Sick sinus syndrome, progressive cardiac conduction disease, atrial flutter and ventricular tachycardia caused by a novel SCN5A mutation. *Cardiology* **115**, 311-316 (2010).

34 Ben-Shalom, R. *et al.* Opposing Effects on $Na_V1.2$ Function Underlie Differences Between SCN2A Variants Observed in Individuals With Autism Spectrum Disorder or Infantile Seizures. *Biol. Psychiatry* **82**, 224-232 (2017).

35 McCormack, K. *et al.* Voltage sensor interaction site for selective small molecule inhibitors of voltage-gated sodium channels. *Proc. Natl. Acad. Sci. U S A* **110**, E2724-2732 (2013).

36 Ahuja, S. *et al.* Structural basis of Nav1.7 inhibition by an isoform-selective small-molecule antagonist. *Science* **350**, aac5464 (2015).

37 Chowdhury, S. *et al.* Discovery of XEN907, a spirooxindole blocker of $Na_V1.7$ for the treatment of pain. *Bioorg. Med. Chem. Lett.* **21**, 3676-3681 (2011).

38 Bregman, H. *et al.* Identification of a potent, state-dependent inhibitor of Nav1.7 with oral efficacy in the formalin model of persistent pain. *J. Med. Chem.* **54**, 4427-4445 (2011).

39 Bregman, H. *et al.* Preparation of aryl carboxamide derivatives as sodium channel inhibitors for treatment of pain. doi:WO 2011103196 A1 (2011).

40 Cummins, T. R., Dib-Hajj, S. D. & Waxman, S. G. Electrophysiological properties of mutant Nav1.7 sodium channels in a painful inherited neuropathy. *J. Neurosci.* **24**, 8232-8236 (2004).

41 Chanda, B. & Bezanilla, F. Tracking voltage-dependent conformational changes in skeletal muscle sodium channel during activation. *J. Gen. Physiol.* **120**, 629-645 (2002).

42 Sun, J. *et al.* Novel *SCN9A* missense mutations contribute to congenital insensitivity to pain: Unexpected correlation between electrophysiological characterization and clinical phenotype. *Mol. Pain* **16**, 1744806920923881 (2020).

43 Favre, I., Moczydlowski, E. & Schild, L. On the structural basis for ionic selectivity among Na^+, K^+, and Ca^{2+} in the voltage-gated sodium channel. *Biophys. J.* **71**, 3110-3125 (1996).

44 Zhao, Y. *et al.* Molecular Basis for Ligand Modulation of a Mammalian Voltage-Gated Ca^{2+} channel. *Cell* **177**, 1495-1506.e1412 (2019).

45 Zhao, Y. *et al.* Cryo-EM structures of apo and antagonist-bound human $Ca_V3.1$. *Nature* **576**, 492-497 (2019).

46 Ragsdale, D. S., McPhee, J. C., Scheuer, T. & Catterall, W. A. Common molecular determinants of local anesthetic, antiarrhythmic, and anticonvulsant block of voltage-gated Na^+ channels. *Proc. Natl. Acad. Sci. U S A* **93**, 9270-9275 (1996).

47 Li, Z. *et al.* Structural Basis for Pore Blockade of the Human Cardiac Sodium Channel Nav1.5 by the Antiarrhythmic Drug Quinidine. *Angew. Chem. Int. Ed. Engl.* **60**, 11474-11480 (2021).

48 Catterall, W. A., Lenaeus, M. J. & Gamal El-Din, T. M. Structure and Pharmacology of Voltage-Gated Sodium and Calcium Channels. *Annu. Rev. Pharmacol. Toxicol.* **60**, 133-154 (2020).

49 Catterall, W. A. *et al.* Voltage-gated ion channels and gating modifier toxins. *Toxicon* **49** (2007).

50 Li, X. *et al.* Structural basis for modulation of human $Na_V1.3$ by clinical drug and selective antagonist. *Nat Commun* **13**, 1286 (2022).

51 Noreng, S., Li, T. & Payandeh, J. Structural Pharmacology of Voltage-Gated Sodium Channels. *J. Mol. Biol.* **433**, 166967 (2021).

Methods

Whole-cell Voltage-clamp recordings of $Na_V1.3$ in HEK 293T Cells

HEK293T cells were cultured with Dulbecco's Modified Eagle Medium (DMEM) (GIBCO, USA) supplemented with 15% (v/v) fetal bovine serum (FBS) (PAN-Biotech, Germany) at 37℃ with 5% CO_2. The cells were seeded in culture dishes (d = 3.5 cm) (Thermo Fisher Scientific, USA) for 24 h, then each dish was transiently transfected with 1 μg plasmids of human $Na_V1.7$ using 1 μg Lipofectamine 2000 Reagent (Thermo Fisher Scientific, USA). Whole-cell voltage-clamp recordings were carried out similarly to our previous study[52]. In brief, transfected cells were placed on a glass chamber with extracellular solution containing 140 mM NaCl, 3 mM KCl, 10 mM HEPES, 10 mM D-Glucose, 1 mM $MgCl_2$, 1 mM $CaCl_2$, (pH = 7.3, adjusted with NaOH; osmolarity of ~310 $mosmol^{-1}$). Recordings were made from isolated, GFP-positive cells using 1.5 ~2.5 MΩ fire polished pipettes (Sutter Instrument, USA) filled with standard internal solution composed of 140mM CsF, 10 mM HEPES, 1 mM EGTA, 10 mM NaCl, (pH = 7.3, adjusted with CsOH; osmolarity of ~300 $mosmol^{-1}$). Currents were recorded using an EPC-10 amplifier (HEKA Elektronik, Germany) at 20 kHz sample rate and was low pass filtered at 5 kHz. The cells with series resistance in the range of 2-6 MΩ were accepted for the further investigations, and the series resistance was compensated by approximately 70-90%. Recordings were discarded if the series resistance was increased to more than 6 MΩ during the course of recording. The data was acquired by PatchMaster program (HEKA Elektronik, Germany).

For pharmacological studies, all antagonists were dissolved in DMSO at 10 mM stock concentration. The antagonist stocks were diluted into extracellular solutions to obtain the desired concentrations. Cells were perfused using a gravity fed system controlled by a VC^3 8 channel valve commander (ALA Scientific Instruments, USA). The final concentration of DMSO in the external solution did not exceed 0.3%.

To characterize the voltage-dependence of activation of $Na_v1.7$, cells were held at -120 mV and then a series of 100 ms test pulses from -80 mV to +40 mV (5 mV increments) were applied. The voltage-dependence of fast inactivation properties of $Na_v1.7$ were assessed with a 500 ms holding-voltages ranging from -120 mV to -20 mV (5 mV increments) followed by a 50 ms test pulse at -5 mV. The recovery from fast inactivation properties were assessed by a double-pulse protocol using a varying interval between the two voltage pulses. Holding potential was set at –120 mV followed a pre-pulse at –5 mV for 20 ms, then a recovery test pulse of –5 mV for 20 ms at 1 to 128 ms. The currents elicited by the test pulse were normalized to construct the recovery curve. The antagonist effect on recovery was evaluated using a protocol in which each cell was clamped at -120 mV or -80 mV and after 20 ms recovery of -150 mV, currents were elicited by a 20 ms test pulse at -5 mV. The sodium currents elicited by this test pulse were sampled every 30 s.

As for the voltage-clamp recording analyses, all data were reported as mean ± s.e.m. Data were analyzed using Origin 2019b (OriginLab, USA), Excel 2016 (Microsoft, USA), and GraphPad Prism 8.0.2 (GraphPad Software, USA).

Steady-state activation curves were generated using a Boltzmann equation.

$$\frac{G}{G_{max}} = \frac{1}{1 + \exp[(V - V_{0.5})/k]}$$

Where G is the conductance, G_{max} is the maximal conductance of $Na_v1.7$ during the protocol, V is the test potential, $V_{0.5}$ is the half-maximal activation potential and k is the slope factor.

Fast inactivation curves were generated using a Boltzmann equation.

$$\frac{I}{I_{max}} = \frac{1}{1 + \exp[(V - V_{0.5})/k]}$$

Where I is the current at indicated test pulse, I_{max} is the maximal current of $Na_V1.7$ activation during test-pulse, V is the test potential, $V_{0.5}$ is the half-maximal inactivation potential and k is the slope factor.

Recovery curves from fast inactivation were fit using a single exponential of the following equation.

$$\frac{I_{test}}{I_{pre}} = (y_0 - 1) * \exp\left(-\frac{t}{\tau}\right) + 1$$

Where I_{pre} is the current at pre-pulse, I_{test} is the current at test pulse, y_0 is the non-inactivated current at the first pulse, t is the delay time between pre-pulse and test-pulse, and τ is the time constant of recovery from fast inactivation.

Concentration response curves were generated from at least 5 different test concentrations (n≥ 5) using logistic equation:

$$\frac{I_{drug}}{I_{max}} = \frac{1}{(1 + 10^{((logIC_{50} - X) * Hillslope)})}$$

Where X is the log of concentrations and IC_{50} is the concentration producing a half-maximum inhibition.

Expression and purification of human $Na_V1.7$/β1/β2 complex

The genes of human $Na_V1.7$ alternative splicing variant 3 (Uniprot accession: 15858-3, splicing isoform 3, missing V648-S658, the residue coordinates are named in consistency with isoform 1; forward primer: gatggcaatgttgcctcccccag, reverse primer: caaaaatgaagctctatttttgctttc), β1 (Uniprot accession: Q07699; forward primer: ACAGCTCTTAAGGGATCCCGGTCCGatggggaggctgctggcctta, reverse primer: GGAACAGAACTTCCAGTGCGGCCGCttcggccacctggacgcccgtg) and β2 (Uniprot accession: O60939; forward primer: ACAGCTCTTAAGGGATCCCGGTCCGatgcacagagatgcctggcta, reverse primer: TTGTCGAGACTGCAGGCTCTAGATCActtggcgccatcatccgggttgccttc) were amplified

from a human cDNA library, which were subcloned into a modified pEG BacMam vector. A green fluorescent protein (GFP) and a Twin-Strep tag were fused to the C-terminus of $Na_V1.7$ to facilitate protein expressing and purification. All constructs were confirmed by DNA sequencing. The $Na_V1.7$/β1/β2 complex were expressed and purified similarly to our previous studies with modification[50,52]. Recombinant baculoviruses were produced in *Sf*9 insect cells using the Bac-to-Bac baculovirus expression system (Invitrogen, USA). The *Sf*9 cells were cultured in ESF 921 medium (Expression Systems, USA) at 26 °C. HEK293F (GIBCO, USA) cells were cultured in OPM-293 medium (OPM, China) supplemented with 1% (v/v) fetal bovine serum (FBS, PAN, Germany) in a 37 °C incubator with 5% CO_2. When the cell density reaches 2.5×10^6 cells/ml, P2 viruses of $Na_V1.7$, β1 and β2 were added to the medium at ratio of 1:100 (v/v), 1:100 (v/v), and 1:100 (v/v), respectively. After 12 hours, 10 mM sodium butyrate (Sigma, USA) was added to the culture to boost protein expression. The cells were incubated for another 48 hours before harvesting. Then the cells were collected and stored in -80 °C freezer.

For each prep, cell pellets from 1.5-liter cell culture were resuspended in buffer A (20 mM HEPES, 150 mM NaCl, 10 μM XEN907 (MCE, USA), 2 mM β-mercaptoethanol (β-ME), pH 7.5, and protease inhibitor cocktail including 1 mM phenylmethyl-sulfonyl fluoride (PMSF), 0.8 μM pepstatin, 2 μM leupeptin, 2 μM aprotinin and 1 mM benzamidine). Then the cells were homogenized in a Dounce homogenizer and the membrane fraction was collected by ultra-centrifugation at 100,000x g for 45 min. The membrane fraction was resuspended in buffer B (buffer A supplemented with 1% (w/v) n-Dodecyl-β-D-maltoside (DDM, Anatrace, USA), 0.15% (w/v) cholesteryl hemisuccinate (CHS, Anatrace, USA), 5 mM $MgCl_2$ and 1 mM ATP) and was gently agitated at 4 °C for 2 hours. The insoluble fractions were removed by ultra-centrifugation at 100,000x g for 40 minutes. Then the supernatant was loaded onto Streptavidin beads (Smart-Lifesciences, China), which was pre-equilibrated with buffer C (buffer A supplemented with 5mM $MgCl_2$, 5 mM ATP and 0.06% (w/v) Glyco-diosgenin (GDN, Anatrace, USA)). Subsequently, the Streptavidin

Beads were washed with 10 column volumes of buffer C and buffer D (buffer C without 5 mM $MgCl_2$ and 5 mM ATP), respectively. The protein complex was eluted by 5 ml buffer E (buffer D plus 5 mM desthiobiotin). In order to form the $Na_V1.7$-β1-β2-XEN907 complex, the eluted protein sample was supplemented with 100 μM XEN907, and was concentrated using a 100-kDa cut-off concentrator (Merck Millipore, Germany). Finally, the concentrated sample was loaded onto Superose 6 Increase 10/300 GL (GE healthcare, USA) pre-equilibrated with 20 mM HEPES, 150 mM NaCl, 0.007% GDN (w/v) and 2 mM β-ME, pH 7.5. Peak fractions were pooled and concentrated to 5.7 mg/ml. Before cryo-EM sample preparation, additional XEN907 was added to the concentrated sample at a final concentration of 100 μM.

For $Na_V1.7$/β1/β2-TC-N1752 and $Na_V1.7$/β1/β2-$Na_V1.7$-IN2 complexes, the protein samples were purified similarly. The only difference was that XEN907 was replaced by TC-N1752 or Nav1.7-IN2 respectively.

Cryo-EM sample preparation and data collection

Aliquots of 2.5 μl purified $Na_V1.7$ complexes at concentrations of approximately 5-10 mg/ml were placed on glow-discharged holey cooper grids (Quantifoil Cu R1.2/1.3, 300 mesh, Germany), which were blotted for 2.0-4.5 s and plunge-frozen in liquid ethane cooled by liquid nitrogen using a FEI Mark IV Vitrobot (ThermoFisher, USA) at 4 °C with 100% humidity. All data were acquired using a Titan Krios transmission electron microscope (ThermoFisher, USA) operated at 300 kV, equipped with a Gatan K2 Summit direct detector (Gatan, USA) and Gatan Quantum GIF energy filter (Gatan, USA) with a slit width of 20 eV. All movie stacks were manually screened and automatically collected using SerialEM at a calibrated magnification of 105,000 with a physical pixel size of 1.04 Å (super-resolution mode). Defocus range was set between −1.2 and −2.2 μm. The dose rate was adjusted to 10 counts/pixel/s. A total of 2,900, 2,601 and 4,430 movie stacks were collected for $Na_V1.7$-β1-β2-XEN907, $Na_V1.7$-β1-β2-TC-N1752 and $Na_V1.7$-β1-β2-

IN-2, respectively. Each movie stack was exposed for 6.4 s fractionated into 32 frames with a total dose of 60 e^-/ Å^2.

Data processing

The movie stacks were motion-corrected, binned by 2-fold and dose-weighted using MotionCorr2 [53], generating summed micrographs for particle picking. Defocus values of each micrographs were estimated using Gctf[54] using the non-dose-weighted micrographs. A total of 1,217,568, 1,216,370 and 1,849,983 particles were auto-picked for $Na_V1.7$-β1-β2-XEN907, $Na_V1.7$-β1-β2-TC-N1752 and $Na_V1.7$-β1-β2-IN2, respectively. All 2D classification, 3D classification, polishing and CTF refinement were carried out in RELION3.0[55]. After polishing, the best class containing 213,507, 158,142 and 206,251 particles for $Na_V1.7$-β1-β2-XEN907, $Na_V1.7$-β1-β2-TC-N1752 and $Na_V1.7$-β1-β2-IN2 were refined using cryoSPARC[56] to 3.22 Å, 3.09 Å and 3.07 Å, respectively. The detailed data processing flowchart was shown in Extended Data Fig. 3.

Model building

The structure of human $Na_V1.7$ (PDB code: 6j8j) was manually fitted into the EM map of $Na_V1.7$-β1-β2-XEN907 in Chimera[57]. To build the NTD model, the AlphaFold2 model of the $Na_V1.7$ NTD was manually fitted in the EM map of the $Na_V1.7^{XEN}$, after several iterations of manual checking and real-space refinement, flexible loop regions without density were removed, yielding the final NTD model containing P7-R30 and P49-S113. Each model was manually checked and corrected in COOT[58], and then refined in Phenix[59]. The model vs map FSC curves were generated by Phenix.real_sapce_refine using Phenix. The statistics of cryo-EM data collection and model refinement were summarized in Table 1. All figures were prepared with PyMOL (Schrödinger, LLC), and Prism 8.0.1 (GraphPad Software) and ChimeraX[60].

Data Availability

The Uniprot accession codes for the sequences of human Nav1.7, β1 and β2 are Q15858-3 [https://www.uniprot.org/uniprot/Q15858-3], Q07699 [https://www.uniprot.org/uniprot/Q07699], and O60939 [https://www.uniprot.org/uniprot/O60939], respectively. The accession codes for the coordinates of Nav1.7, Nav1.5-Flecainide, Nav1.5-Propafenone and Nav1.5-Qunidine used in this study are 6J8J [http://doi.org/10.2210/pdb6J8J/pdb], 6UZ0 [http://doi.org/10.2210/pdb6UZ0/pdb], 7FBS [http://doi.org/10.2210/pdb7FBS/pdb], and 6LQA [http://doi.org/10.2210/pdb6LQA/pdb], respectively. The accession code for the EM map of Nav1.7 used in this study is EMD-9782 [https://www.emdataresource.org/EMD-9782]. The three-dimensional cryo-EM density maps of the human $Na_V1.7$-β1-β2-XEN907, $Na_V1.7$-β1-β2-TC-N1752 and $Na_V1.7$-β1-β2-$Na_V1.7$-IN2 have been deposited in the EM Database under accession codes EMD-33292 [https://www.emdataresource.org/EMD-33292], EMD-33295 [https://www.emdataresource.org/EMD-33295], and EMD-33296 [https://www.emdataresource.org/EMD-33296], respectively. The coordinates of the $Na_V1.7$-β1-β2-XEN907, $Na_V1.7$-β1-β2-TC-N1752 and $Na_V1.7$-β1-β2-$Na_V1.7$-IN2 have been deposited in the Protein Data Bank under accession codes 7XM9 [http://doi.org/10.2210/pdb7XM9/pdb], 7XMF [http://doi.org/10.2210/pdb7XMF/pdb], and 7XMG [http://doi.org/10.2210/pdb7XMG/pdb], respectively. Source Data are provided with this paper.

Methods-only References

52 Zhang, J. *et al.* N-type fast inactivation of a eukaryotic voltage-gated sodium channel. *Nat Commun* **13**, 2713 (2022).

53 Zheng, S. Q. *et al.* MotionCor2: anisotropic correction of beam-induced motion for improved cryo-electron microscopy. *Nat Methods* **14**, 331-332 (2017).

54 Zhang, K. Gctf: Real-time CTF determination and correction. *J Struct Biol* **193**, 1-12 (2016).

55 Zivanov, J. *et al.* New tools for automated high-resolution cryo-EM structure determination in RELION-3. *Elife* **7** (2018).

56 Punjani, A., Rubinstein, J. L., Fleet, D. J. & Brubaker, M. A. cryoSPARC: algorithms for rapid unsupervised cryo-EM structure determination. *Nat Methods* **14**, 290-296 (2017).

57 Pettersen, E. F. *et al.* UCSF Chimera--a visualization system for exploratory research and analysis. *J Comput Chem* **25**, 1605-1612 (2004).
58 Emsley, P. & Cowtan, K. Coot: model-building tools for molecular graphics. *Acta Crystallogr D Biol Crystallogr* **60**, 2126-2132 (2004).
59 Adams, P. D. *et al.* PHENIX: a comprehensive Python-based system for macromolecular structure solution. *Acta Crystallogr D Biol Crystallogr* **66**, 213-221 (2010).
60 Pettersen, E. F. *et al.* UCSF ChimeraX: Structure visualization for researchers, educators, and developers. *Protein Sci* **30**, 70-82 (2021).

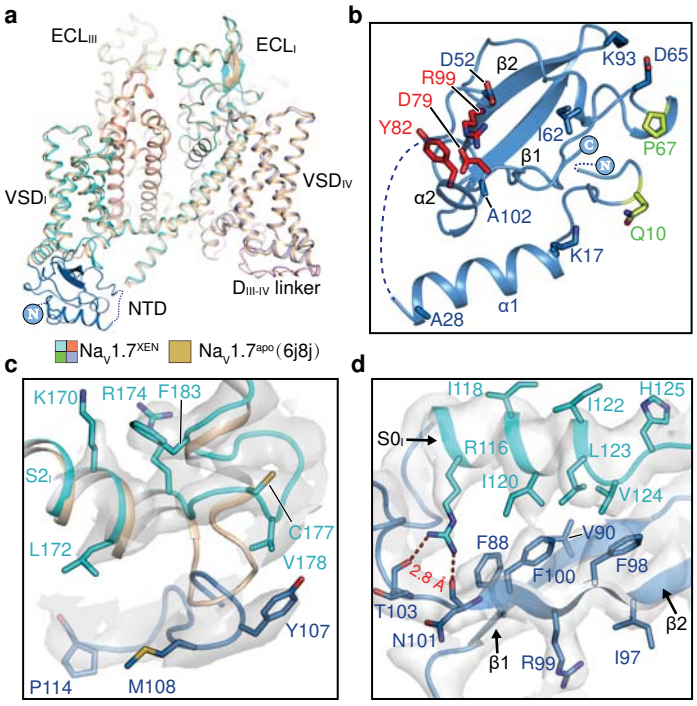
a
ECL$_{III}$
ECL$_{I}$
VSD$_{I}$
VSD$_{IV}$
D$_{III-IV}$ linker
NTD
N
Na$_V$1.7^{XEN}
Na$_V$1.7^{apo}(6j8j)
b
D52
β2
K93
D65
R99
D79
Y82
I62
P67
β1
C
N
α2
A102
Q10
K17
A28
α1
c
K170
R174
F183
S2$_{I}$
C177
L172
V178
Y107
P114
M108
d
I118
I122
H125
S0$_{I}$
R116
L123
I120
V124
V90
F88
F98
F100
2.8 Å
T103
β2
N101
β1
R99
I97

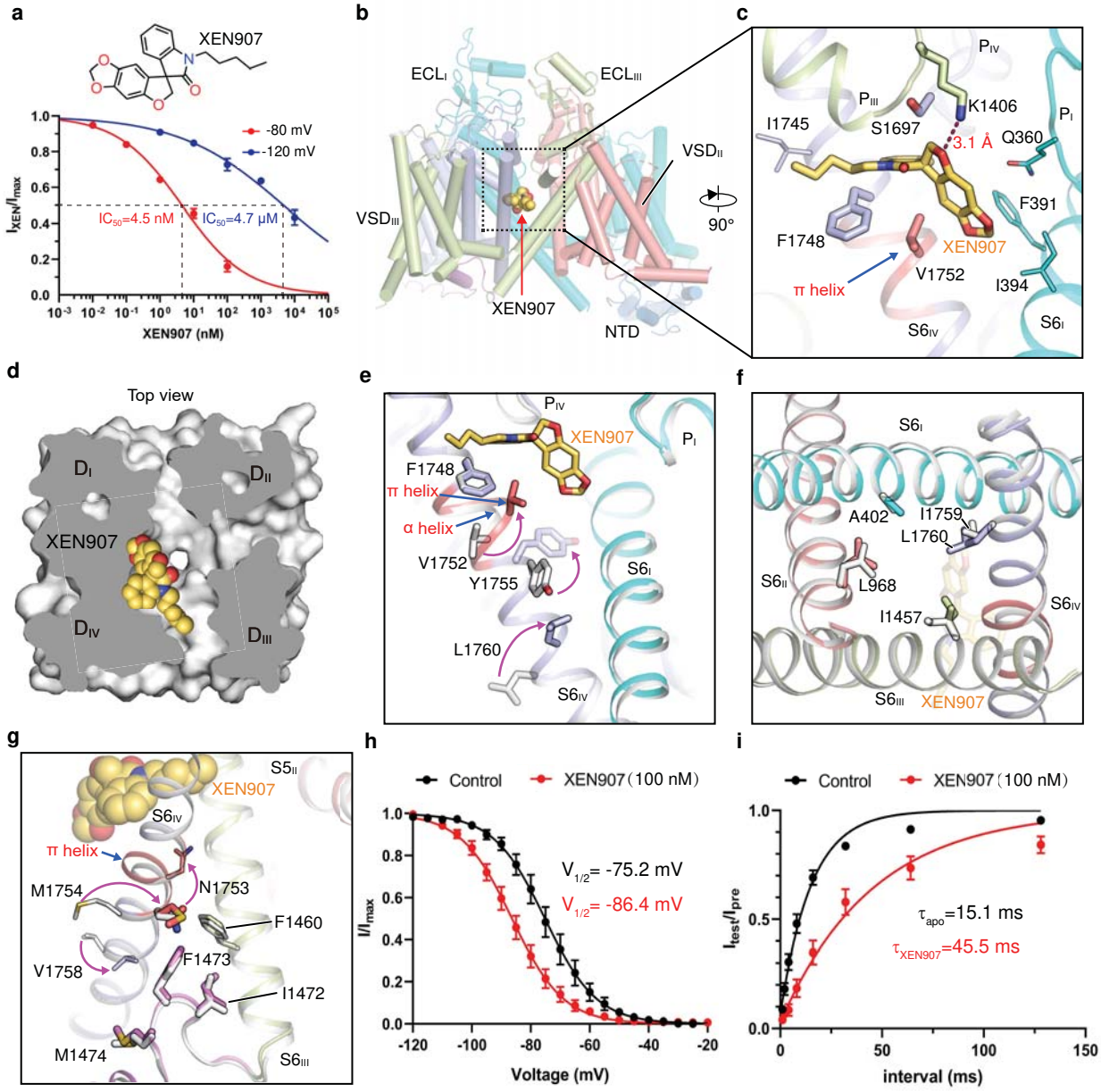
a
XEN907
-80 mV
-120 mV
IC50=4.5 nM
IC50=4.7 μM
IXEN/Imax
XEN907 (nM)
b
ECLI
ECLIII
VSDII
VSDIII
90°
XEN907
NTD
c
PIV
PIII
K1406
PI
I1745
S1697
3.1 Å
Q360
F391
F1748
XEN907
π helix
V1752
I394
S6IV
S6I
d
Top view
DI
DII
XEN907
DIV
DIII
e
PIV
XEN907
PI
F1748
π helix
α helix
V1752
Y1755
S6I
L1760
S6IV
f
S6I
A402
I1759
L1760
S6II
L968
S6IV
I1457
S6III
XEN907
g
S5II
XEN907
S6IV
π helix
M1754
N1753
F1460
F1473
V1758
I1472
M1474
S6III
h
Control
XEN907 (100 nM)
V1/2= -75.2 mV
V1/2= -86.4 mV
I/Imax
Voltage (mV)
i
Control
XEN907 (100 nM)
τapo=15.1 ms
τXEN907=45.5 ms
Itest/Ipre
interval (ms)

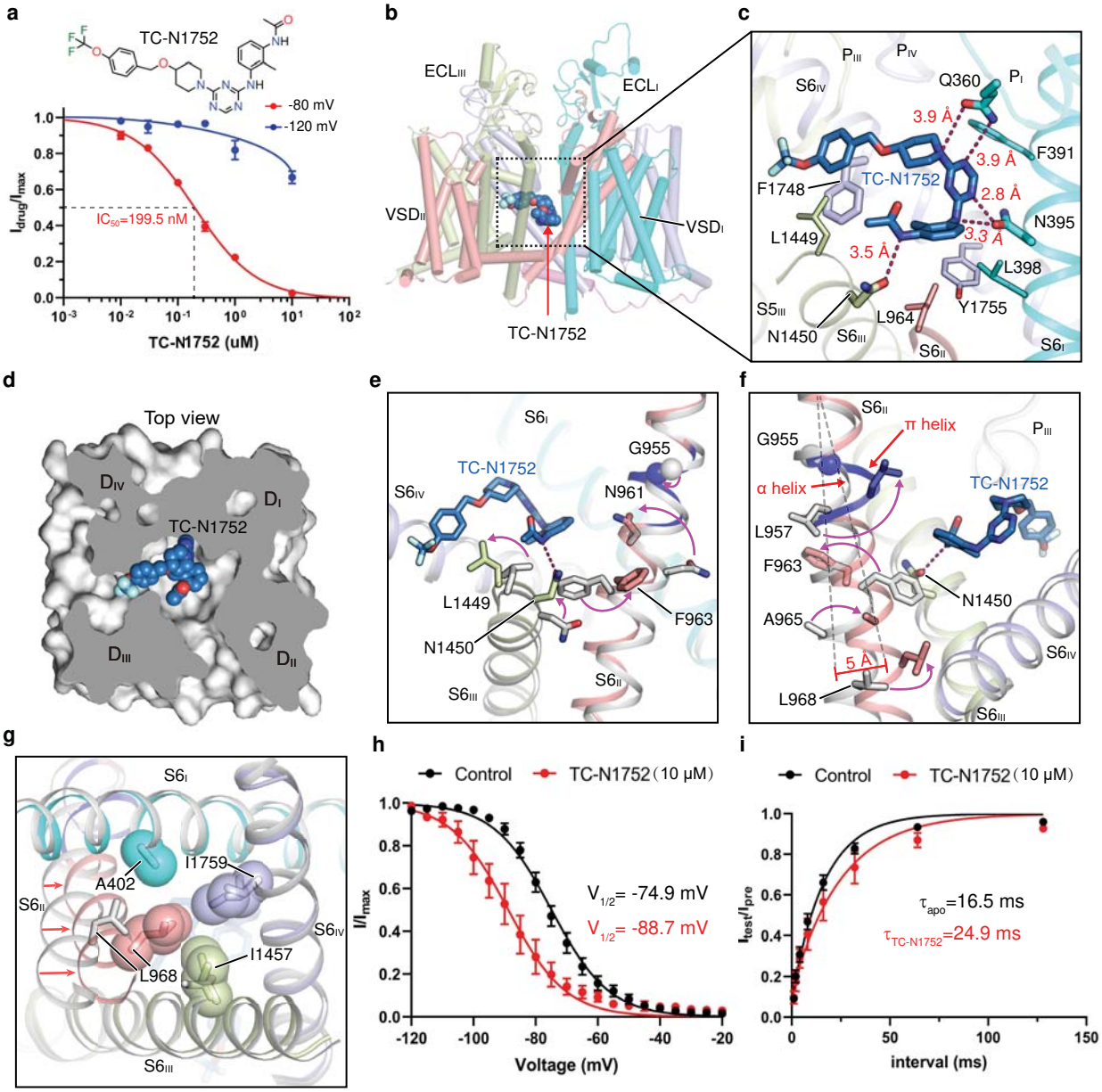
a
TC-N1752
-80 mV
-120 mV
IC50=199.5 nM
I drug/I max
TC-N1752 (uM)
b
ECLIII
ECLI
VSDII
VSDI
TC-N1752
c
PIII
PIV
S6IV
Q360
PI
3.9 Å
F391
3.9 Å
F1748
TC-N1752
2.8 Å
N395
L1449
3.3 Å
3.5 Å
L398
S5III
L964
Y1755
N1450
S6III
S6II
S6I
d
Top view
DIV
DI
TC-N1752
DIII
DII
e
S6I
G955
TC-N1752
S6IV
N961
L1449
F963
N1450
S6III
S6II
f
S6II
π helix
PIII
G955
α helix
TC-N1752
L957
F963
N1450
A965
5 Å
S6IV
L968
S6III
g
S6I
I1759
A402
S6II
S6IV
I1457
L968
S6III
h
Control
TC-N1752 (10 μM)
I/I max
V1/2= -74.9 mV
V1/2= -88.7 mV
Voltage (mV)
i
Control
TC-N1752 (10 μM)
I test/I pre
τapo=16.5 ms
τTC-N1752=24.9 ms
interval (ms)

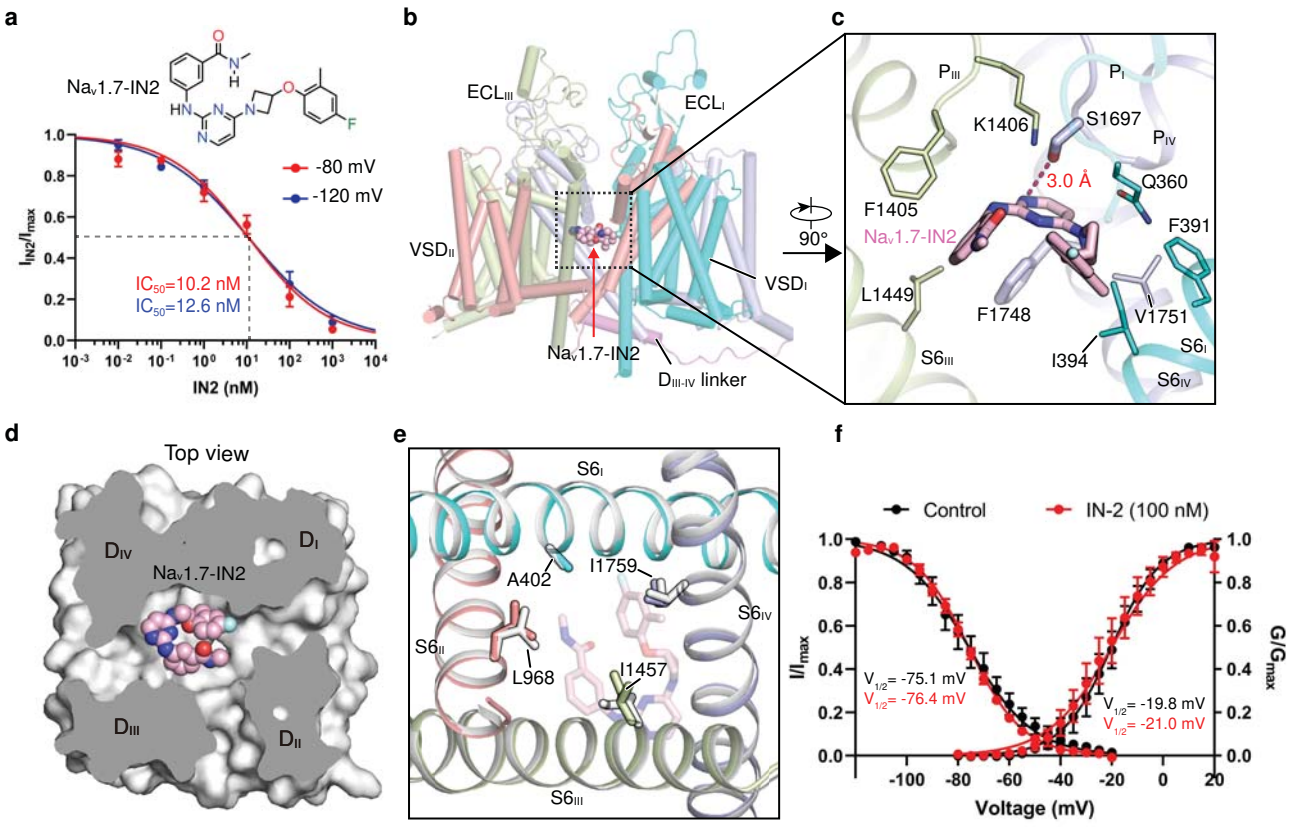
a
Nav1.7-IN2
-80 mV
-120 mV
IC50=10.2 nM
IC50=12.6 nM
IN2 (nM)
b
ECLIII
ECLI
VSDII
VSDI
Nav1.7-IN2
DIII-IV linker
90°
c
PIII
PI
K1406
S1697
PIV
3.0 Å
Q360
F1405
Nav1.7-IN2
F391
L1449
F1748
V1751
S6I
S6III
I394
S6IV
d
Top view
DIV
DI
Nav1.7-IN2
DIII
DII
e
S6I
A402
I1759
S6IV
S6II
L968
I1457
S6III
f
Control
IN-2 (100 nM)
V1/2= -75.1 mV
V1/2= -76.4 mV
V1/2= -19.8 mV
V1/2= -21.0 mV
Voltage (mV)

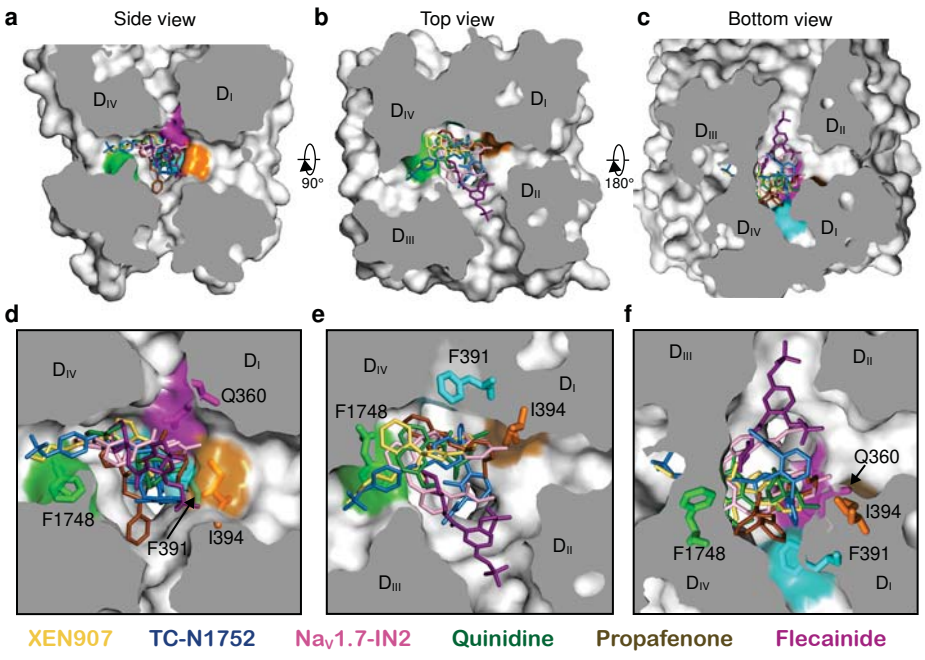
a
Side view
b
Top view
c
Bottom view
DIV
DI
DII
DIII
90°
180°
d
e
f
Q360
F1748
F391
I394
XEN907
TC-N1752
NaV1.7-IN2
Quinidine
Propafenone
Flecainide

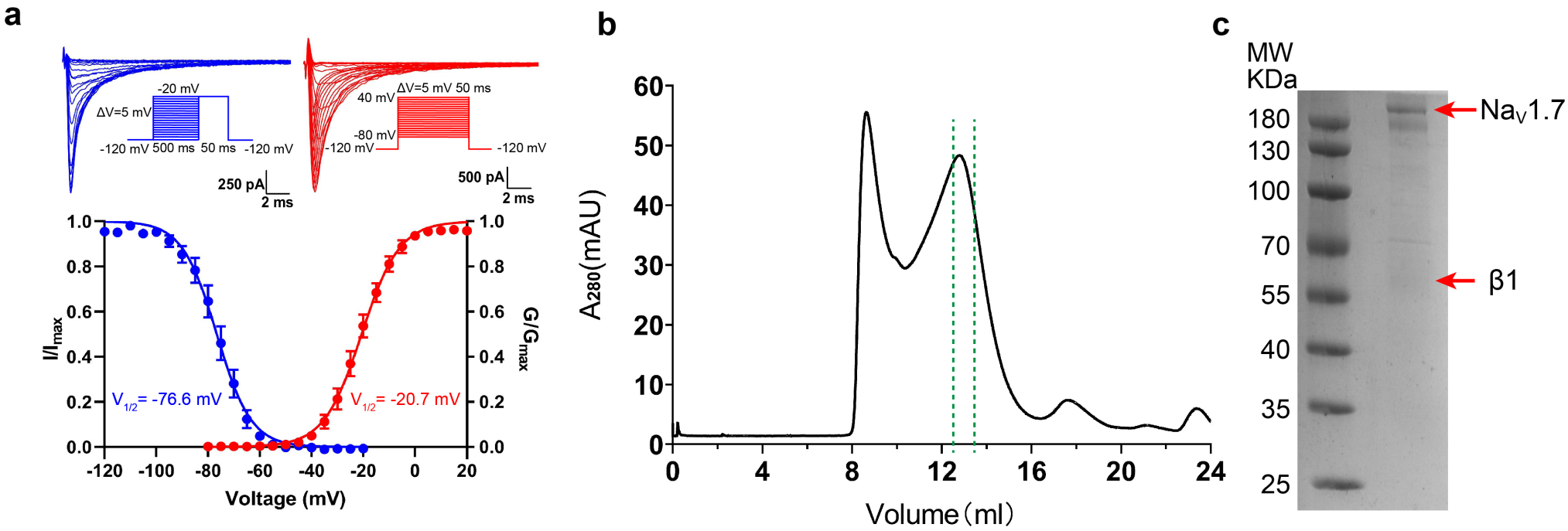
a
-20 mV
ΔV=5 mV
-120 mV 500 ms 50 ms -120 mV
250 pA
2 ms
40 mV
ΔV=5 mV 50 ms
-80 mV
-120 mV
-120 mV
500 pA
2 ms
I/I_max
G/G_max
V_1/2= -76.6 mV
V_1/2= -20.7 mV
Voltage (mV)
b
A280(mAU)
Volume（ml）
c
MW
KDa
180
130
100
70
55
40
35
25
Na_V1.7
β1

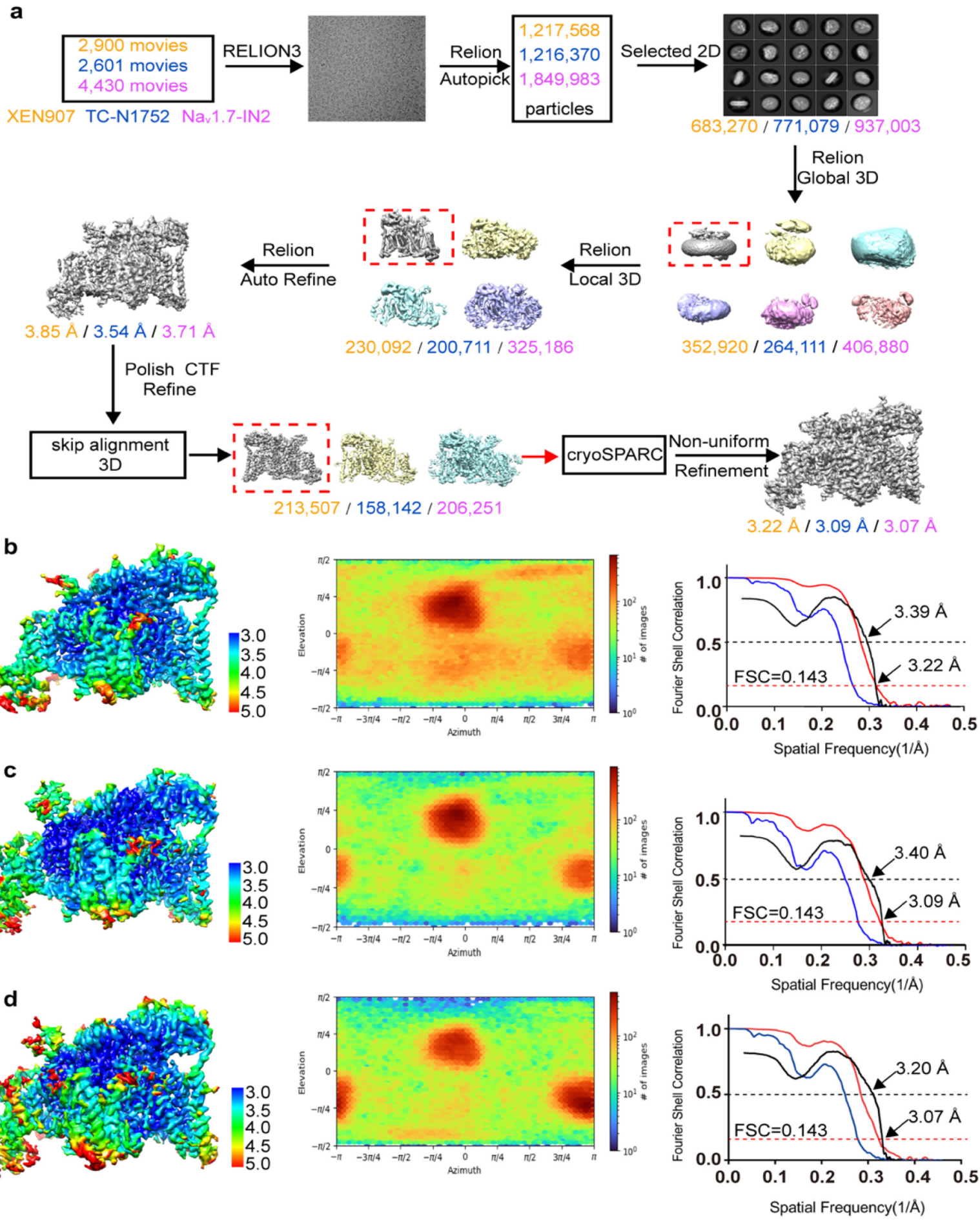
a
2,900 movies
2,601 movies
4,430 movies
XEN907 TC-N1752 Na$_V$1.7-IN2
RELION3
Relion Autopick
1,217,568
1,216,370
1,849,983
particles
Selected 2D
683,270 / 771,079 / 937,003
Relion Global 3D
352,920 / 264,111 / 406,880
Relion Local 3D
230,092 / 200,711 / 325,186
Relion Auto Refine
3.85 Å / 3.54 Å / 3.71 Å
Polish CTF Refine
skip alignment 3D
213,507 / 158,142 / 206,251
cryoSPARC Non-uniform Refinement
3.22 Å / 3.09 Å / 3.07 Å
b
c
d
3.0
3.5
4.0
4.5
5.0
Elevation
Azimuth
# of images
Fourier Shell Correlation
Spatial Frequency(1/Å)
FSC=0.143
3.39 Å
3.22 Å
3.40 Å
3.09 Å
3.20 Å
3.07 Å

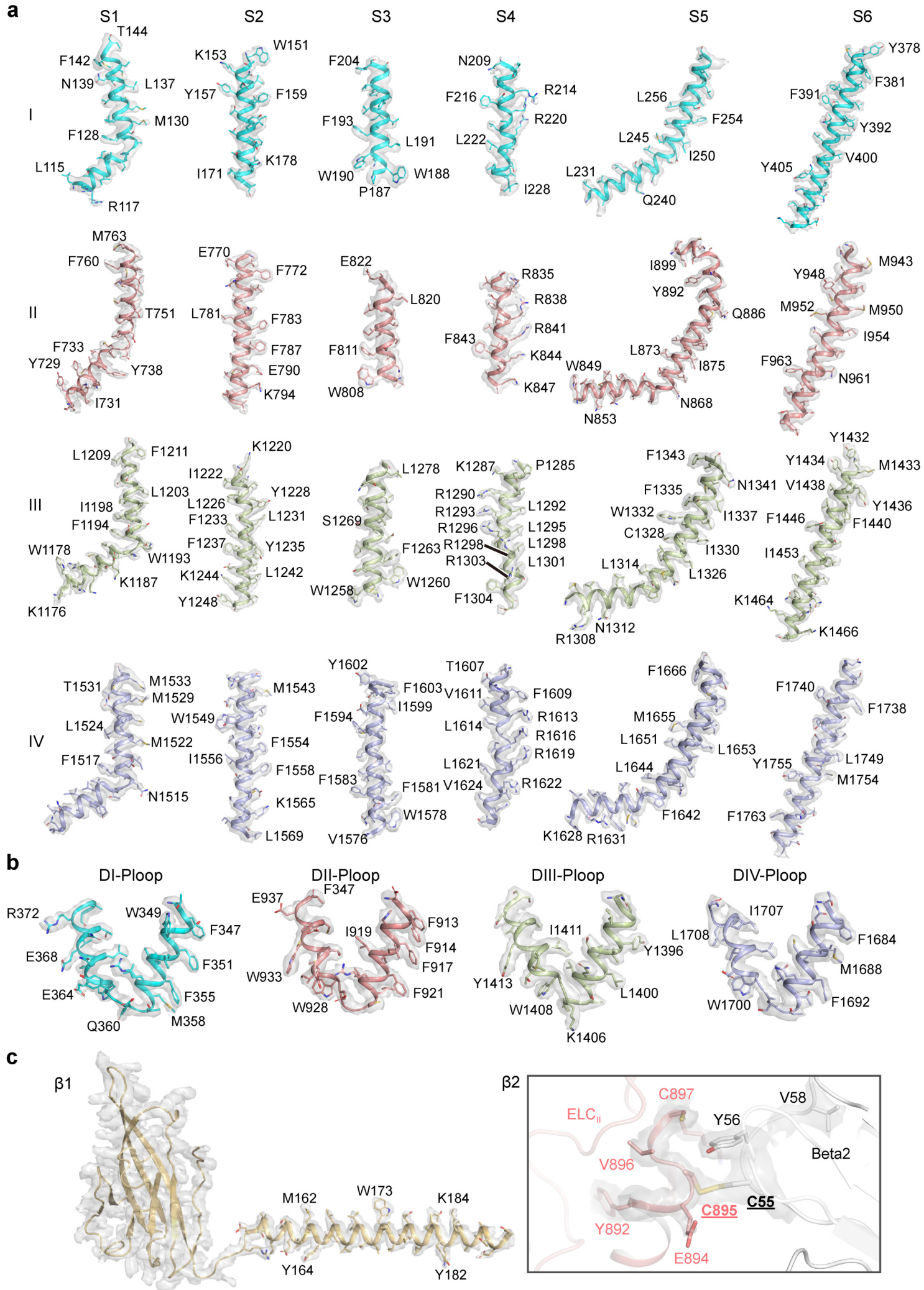
a
S1
S2
S3
S4
S5
S6
I
II
III
IV
T144
F142
N139
L137
M130
F128
L115
R117
K153
W151
Y157
F159
I171
K178
F204
F193
L191
W190
W188
P187
N209
F216
R214
R220
L222
I228
L256
F254
L245
I250
L231
Q240
Y378
F381
F391
Y392
Y405
V400
M763
F760
T751
F733
Y729
Y738
I731
E770
F772
L781
F783
F787
E790
K794
E822
L820
F811
W808
R835
R838
R841
F843
K844
K847
I899
Y892
Q886
L873
I875
W849
N868
N853
Y948
M943
M952
M950
I954
F963
N961
L1209
F1211
L1203
I1198
F1194
W1178
W1193
K1187
K1176
K1220
I1222
Y1228
L1226
L1231
F1233
F1237
Y1235
K1244
L1242
Y1248
L1278
S1269
F1263
W1258
W1260
K1287
P1285
R1290
R1293
R1296
R1298
R1303
L1292
L1295
L1298
L1301
F1304
F1343
N1341
F1335
W1332
I1337
C1328
I1330
L1314
L1326
R1308
N1312
Y1432
Y1434
M1433
V1438
Y1436
F1446
F1440
I1453
K1464
K1466
T1531
M1533
M1529
L1524
M1522
F1517
N1515
M1543
W1549
F1554
I1556
F1558
K1565
L1569
Y1602
F1603
I1599
F1594
F1583
F1581
W1578
V1576
T1607
V1611
F1609
R1613
R1616
R1619
L1614
L1621
V1624
R1622
F1666
M1655
L1651
L1653
L1644
F1642
K1628
R1631
F1740
F1738
Y1755
L1749
M1754
F1763
b
DI-Ploop
DII-Ploop
DIII-Ploop
DIV-Ploop
R372
W349
F347
E368
F351
E364
F355
Q360
M358
E937
F347
I919
F913
F914
F917
W933
F921
W928
I1411
Y1396
L1408
Y1413
L1400
K1406
I1707
L1708
F1684
M1688
W1700
F1692
c
β1
β2
M162
W173
K184
Y164
Y182
C897
ELC$_{II}$
V58
Y56
Beta2
V896
C895
C55
Y892
E894

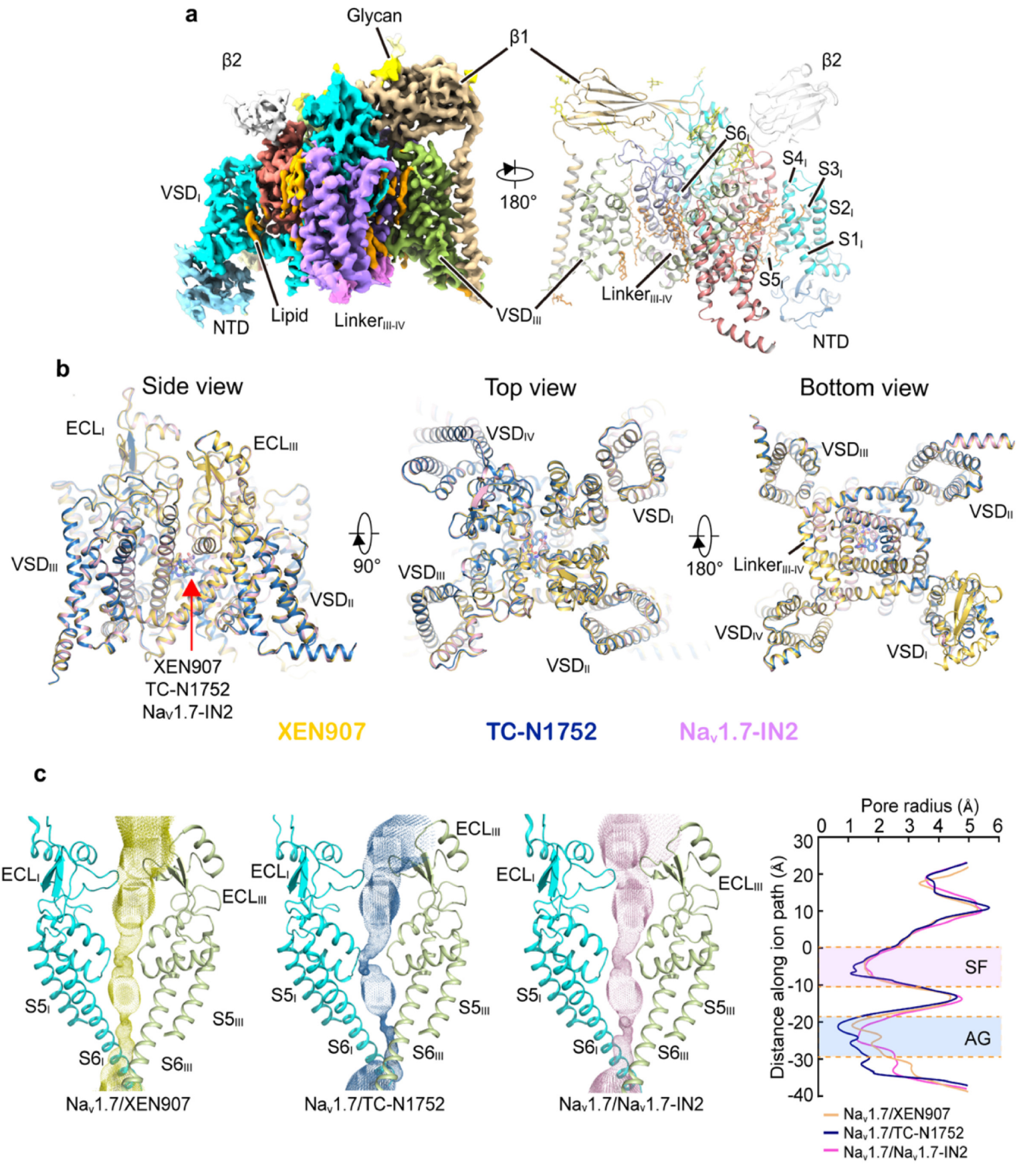
a
Glycan
β1
β2
β2
VSDI
180°
S6I
S4I
S3I
S2I
S1I
S5I
LinkerIII-IV
VSDIII
Lipid
LinkerIII-IV
NTD
NTD
b
Side view
Top view
Bottom view
ECLI
ECLIII
VSDIV
VSDI
VSDIII
VSDII
VSDIII
VSDII
90°
180°
LinkerIII-IV
VSDIV
VSDI
VSDIII
VSDI
VSDII
XEN907
TC-N1752
NaV1.7-IN2
XEN907
TC-N1752
Nav1.7-IN2
c
ECLI
ECLIII
S5I
S5III
S6I
S6III
NaV1.7/XEN907
NaV1.7/TC-N1752
NaV1.7/NaV1.7-IN2
Pore radius (Å)
0 1 2 3 4 5 6
30 20 10 0 -10 -20 -30 -40
Distance along ion path (Å)
SF
AG
NaV1.7/XEN907
NaV1.7/TC-N1752
NaV1.7/NaV1.7-IN2

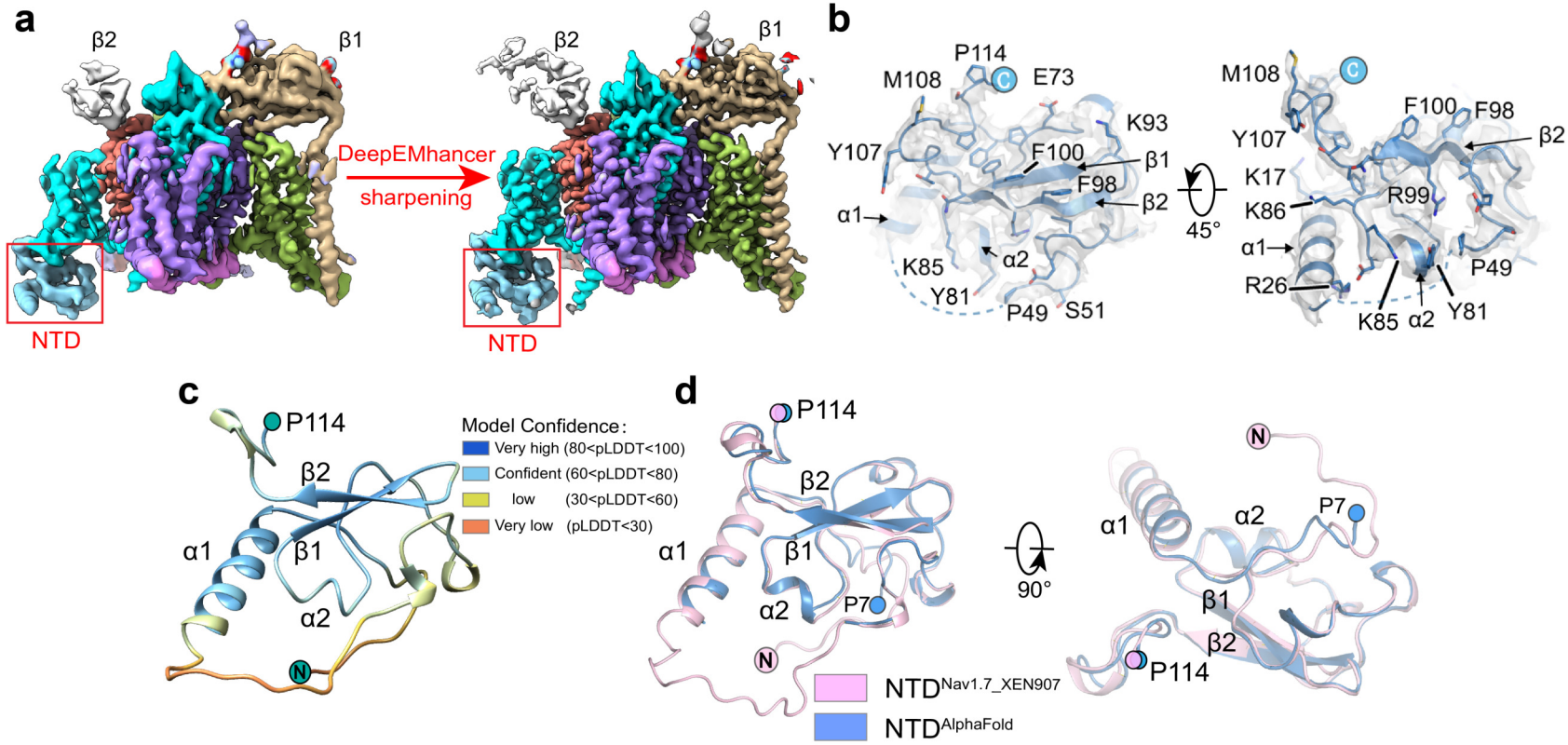

e

α1

```
Nav1.7   1 -----MA--MLPPP---GPQSFVHFTKQSLALIEQRIAERKSKEPKE----EK-KDDDEEAPKPSS  51
Nav1.1   1 ME---QT--VLVPP---GPDSFNFFTRESLAAIERRIAEEKAKNPKP----DK-KDDDENGPKPNS  53
Nav1.2   1 MA---QS--VLVPP---GPDSFRFFTRESLAAIEQRIAEEKAKRPKQ----ERKDEDDENGPKPNS  54
Nav1.3   1 MA---QA--LLVPP---GPESFRLFTRESLAAIEKRAAEEKAKKPKK----EQ-DNDDENKPKPNS  53
Nav1.4   1 MARPSLC--TLVPL---GPECLRPFTRESLAAIEQRAVEEEARLQRN----KQ-MEIEEPERKPRS  56
Nav1.5   1 -M---AN--FLLPR---GTSSFRRFTRESLAAIEKRMAEKQARGSTTLQESRE-GLPEEEAPRPQL  56
Nav1.6   1 MA---AR--LLAPP---GPDSFKPFTPESLANIERRIAESKLKKPPKADGSHR-EDDEDSKPKPNS  57
Nav1.8   1 ---------MEFPIGSLETNNFRRFTPESLVEIEKQIAAKQGTKKARE-KHRE-QKDQEEKPRPQL  55
Nav1.9   1 MD---DRCYPVIFP---DERNFRPFTSDSLAAIEKRIAIQKEKKKSK-----D-QTGEVPQPRPQL  54
```

α2 β1 β2 S0

```
Nav1.7  52 DLEAGKQLPFIYGDIPPGMVSEPLEDLDPYYADKKTFIVLNKGKTIFRFNATPALYMLSPFSPLRR  117
Nav1.1  54 DLEAGKNLPFIYGDIPPEMVSEPLEDLDPYYINKKTFIVLNKGKAIFRFSATSALYILTPFNPLRK  119
Nav1.2  55 DLEAGKSLPFIYGDIPPEMVSVPLEDLDPYYINKKTFIVLNKGKAISRFSATPALYILTPFNPIRK  120
Nav1.3  54 DLEAGKNLPFIYGDIPPEMVSEPLEDLDPYYINKKTFIVMNKGKAIFRFSATSALYILTPLNPVRK  119
Nav1.4  57 DLEAGKNLPMIYGDPPPEVIGIPLEDLDPYYSNKKTFIVLNKGKAIFRFSATPALYLLSPFSVVRR  122
Nav1.5  57 DLQASKKLPDLYGNPPQELIGEPLEDLDPFYSTQKTFIVLNKGKTIFRFSATNALYVLSPFHPIRR  122
Nav1.6  58 DLEAGKSLPFIYGDIPQGLVAVPLEDFDPYYLTQKTFVVLNRGKTLFRFSATPALYILSPFNLIRR  123
Nav1.8  56 DLKACNQLPKFYGELPAELIGEPLEDLDPFYSTHRTFMVLNKGRTISRFSATRALWLFSPFNLIRR  121
Nav1.9  55 DLKASRKLPKLYGDIPRELIGKPLEDLDPFYRNHKTFMVLNRKRTIYRFSAKHALFIFGPFNSIRS  120
```

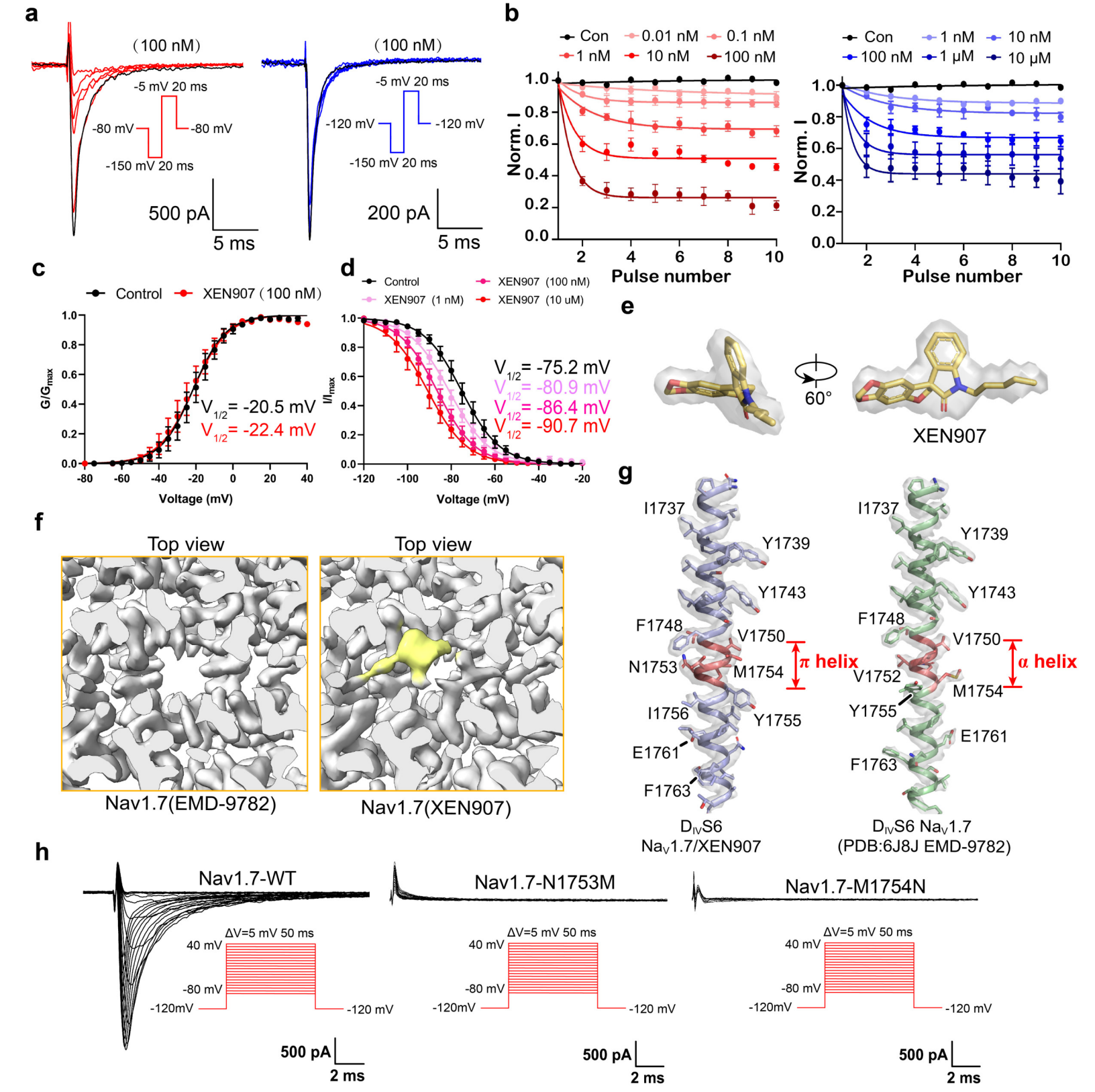
a
(100 nM)
-5 mV 20 ms
-80 mV
-80 mV
-150 mV 20 ms
500 pA
5 ms
(100 nM)
-5 mV 20 ms
-120 mV
-120 mV
-150 mV 20 ms
200 pA
5 ms
b
Con
0.01 nM
0.1 nM
1 nM
10 nM
100 nM
Norm. I
Pulse number
Con
1 nM
10 nM
100 nM
1 μM
10 μM
Norm. I
Pulse number
c
Control
XEN907 (100 nM)
G/Gmax
V1/2= -20.5 mV
V1/2= -22.4 mV
Voltage (mV)
d
Control
XEN907 (1 nM)
XEN907 (100 nM)
XEN907 (10 uM)
I/Imax
V1/2= -75.2 mV
V1/2= -80.9 mV
V1/2= -86.4 mV
V1/2= -90.7 mV
Voltage (mV)
e
60°
XEN907
f
Top view
Top view
Nav1.7(EMD-9782)
Nav1.7(XEN907)
g
I1737
Y1739
Y1743
F1748
V1750
N1753
M1754
π helix
I1756
Y1755
E1761
F1763
DIVS6
NaV1.7/XEN907
I1737
Y1739
Y1743
F1748
V1750
V1752
M1754
α helix
Y1755
E1761
F1763
DIVS6 NaV1.7
(PDB:6J8J EMD-9782)
h
Nav1.7-WT
ΔV=5 mV 50 ms
40 mV
-80 mV
-120mV
-120 mV
500 pA
2 ms
Nav1.7-N1753M
ΔV=5 mV 50 ms
40 mV
-80 mV
-120mV
-120 mV
500 pA
2 ms
Nav1.7-M1754N
ΔV=5 mV 50 ms
40 mV
-80 mV
-120mV
-120 mV
500 pA
2 ms

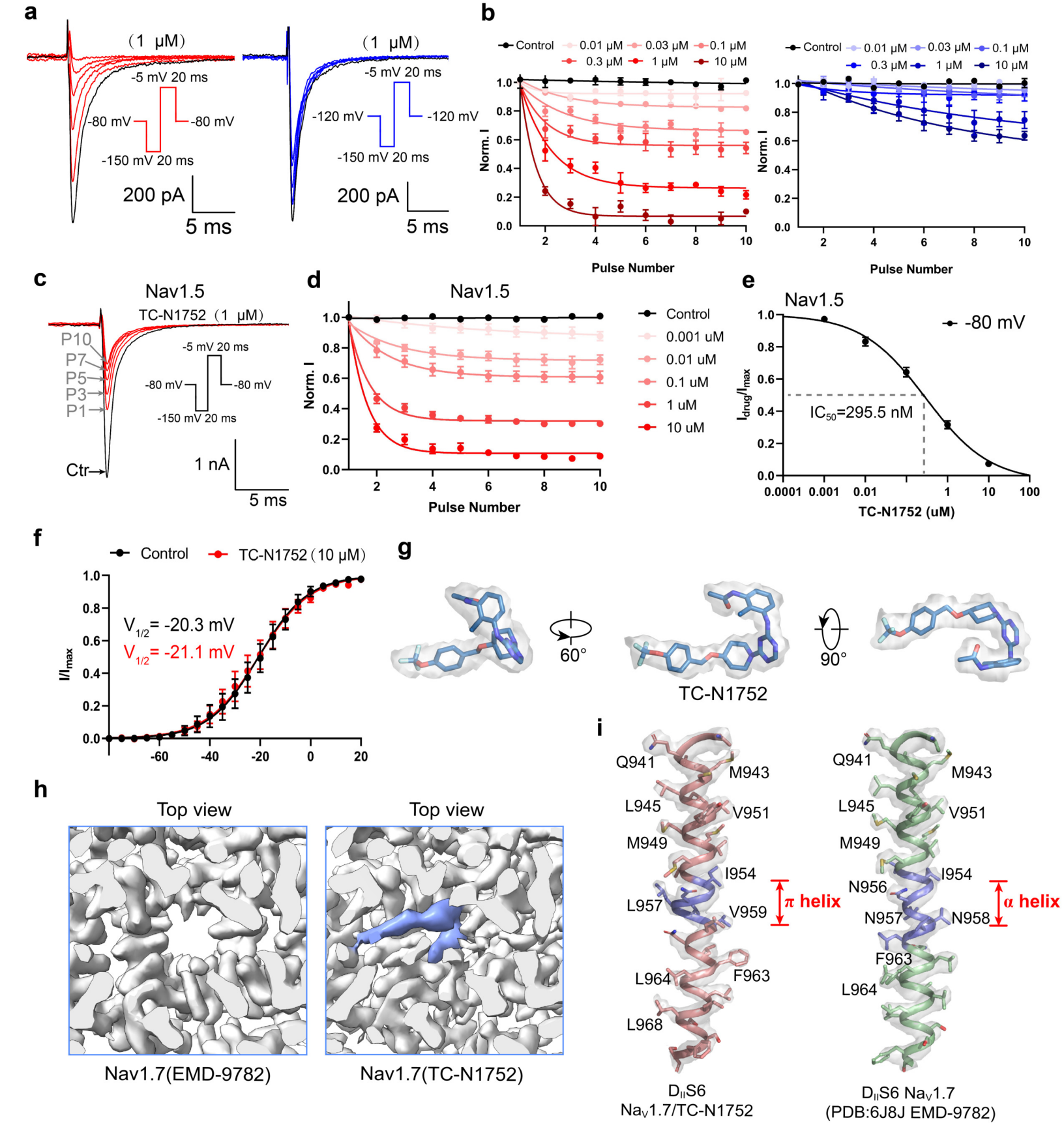
a
(1 μM)
-5 mV 20 ms
-80 mV
-80 mV
-150 mV 20 ms
200 pA
5 ms
(1 μM)
-5 mV 20 ms
-120 mV
-120 mV
-150 mV 20 ms
200 pA
5 ms
b
Control
0.01 μM
0.03 μM
0.1 μM
0.3 μM
1 μM
10 μM
Norm. I
Pulse Number
Control
0.01 μM
0.03 μM
0.1 μM
0.3 μM
1 μM
10 μM
Norm. I
Pulse Number
c
Nav1.5
TC-N1752 (1 μM)
P10
P7
P5
P3
P1
Ctr
-5 mV 20 ms
-80 mV
-80 mV
-150 mV 20 ms
1 nA
5 ms
d
Nav1.5
Norm. I
Pulse Number
Control
0.001 uM
0.01 uM
0.1 uM
1 uM
10 uM
e
Nav1.5
-80 mV
I_{drug}/I_{max}
IC_{50}=295.5 nM
TC-N1752 (uM)
f
Control
TC-N1752 (10 μM)
I/I_{max}
$V_{1/2}$= -20.3 mV
$V_{1/2}$= -21.1 mV
g
60°
90°
TC-N1752
h
Top view
Top view
Nav1.7(EMD-9782)
Nav1.7(TC-N1752)
i
Q941
M943
L945
V951
M949
I954
L957
V959
π helix
L964
F963
L968
$D_{II}S6$
$Na_V1.7$/TC-N1752
Q941
M943
L945
V951
M949
I954
N956
N957
N958
α helix
F963
L964
$D_{II}S6$ $Na_V1.7$
(PDB:6J8J EMD-9782)

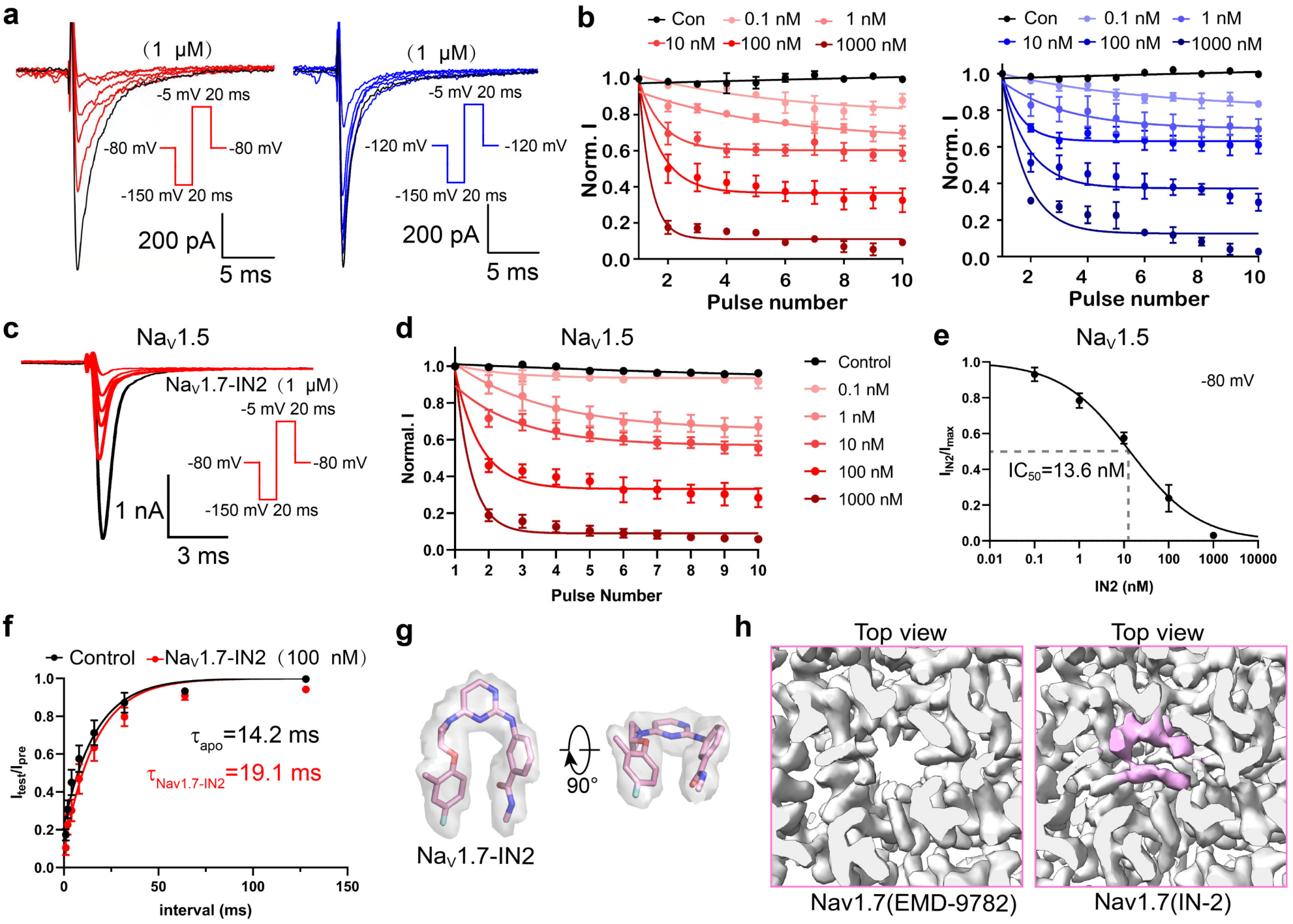
a
(1 μM)
-5 mV 20 ms
-80 mV
-80 mV
-150 mV 20 ms
200 pA
5 ms
(1 μM)
-5 mV 20 ms
-120 mV
-120 mV
-150 mV 20 ms
200 pA
5 ms
b
Con
0.1 nM
1 nM
10 nM
100 nM
1000 nM
Norm. I
Pulse number
Con
0.1 nM
1 nM
10 nM
100 nM
1000 nM
Norm. I
Pulse number
c
NaV1.5
NaV1.7-IN2 (1 μM)
-5 mV 20 ms
-80 mV
-80 mV
-150 mV 20 ms
1 nA
3 ms
d
NaV1.5
Normal. I
Pulse Number
Control
0.1 nM
1 nM
10 nM
100 nM
1000 nM
e
NaV1.5
-80 mV
IC50=13.6 nM
IIN2/Imax
IN2 (nM)
f
Control
NaV1.7-IN2 (100 nM)
τapo=14.2 ms
τNav1.7-IN2=19.1 ms
Itest/Ipre
interval (ms)
g
NaV1.7-IN2
90°
h
Top view
Top view
Nav1.7(EMD-9782)
Nav1.7(IN-2)

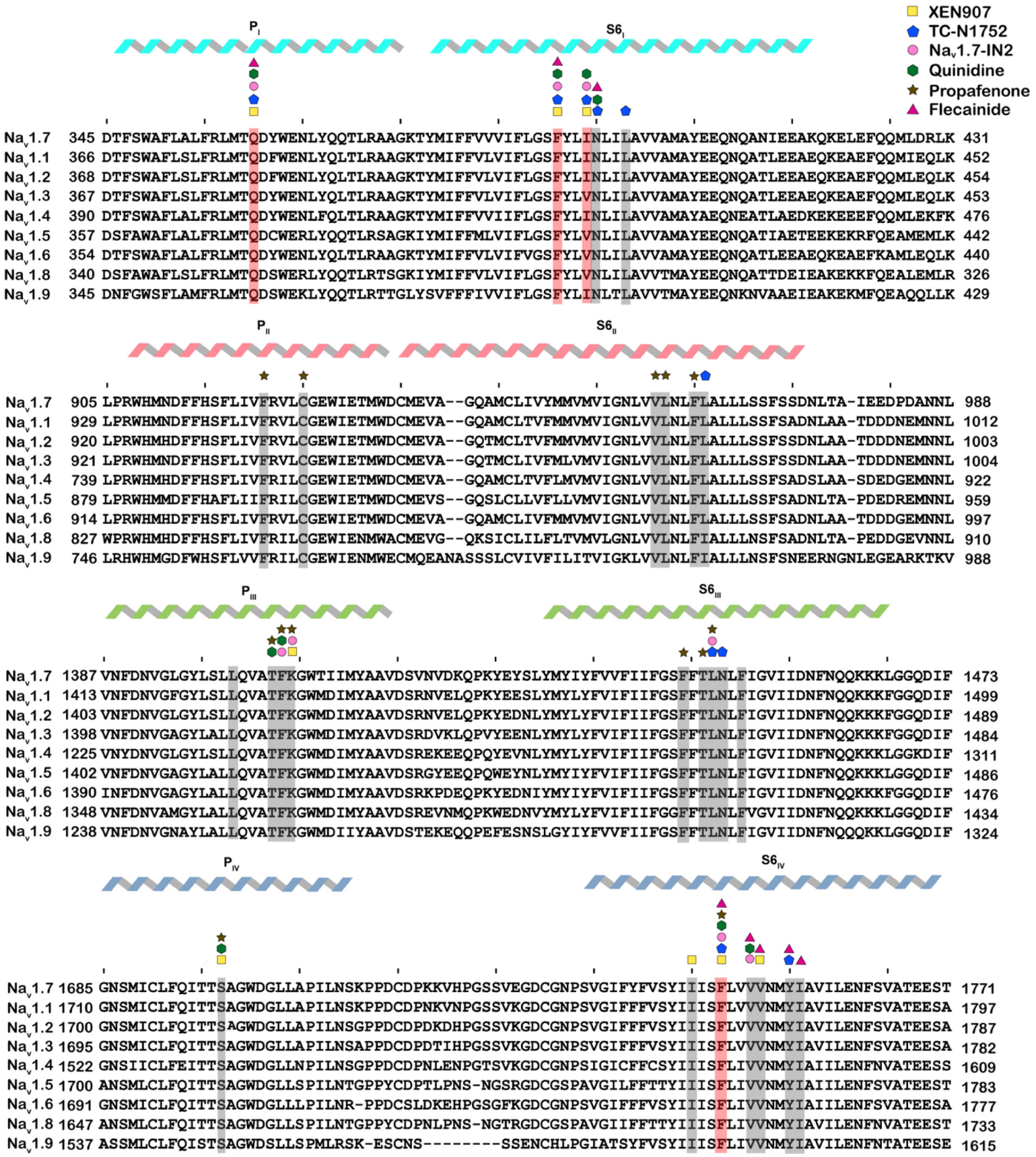
XEN907
TC-N1752
Nav1.7-IN2
Quinidine
Propafenone
Flecainide
PI
S6I
PII
S6II
PIII
S6III
PIV
S6IV
Nav1.7 345 DTFSWAFLALFRLMTQDYWENLYQQTLRAAGKTYMIFFVVVIFLGSFYLINLILAVVAMAYEEQNQANIEEAKQKELEFQQMLDRLK 431
Nav1.1 366 DTFSWAFLSLFRLMTQDFWENLYQLTLRAAGKTYMIFFVLVIFLGSFYLINLILAVVAMAYEEQNQATLEEAEQKEAEFQQMIEQLK 452
Nav1.2 368 DTFSWAFLSLFRLMTQDFWENLYQLTLRAAGKTYMIFFVLVIFLGSFYLINLILAVVAMAYEEQNQATLEEAEQKEAEFQQMLEQLK 454
Nav1.3 367 DTFSWAFLSLFRLMTQDYWENLYQLTLRAAGKTYMIFFVLVIFLGSFYLVNLILAVVAMAYEEQNQATLEEAEQKEAEFQQMLEQLK 453
Nav1.4 390 DTFSWAFLALFRLMTQDYWENLFQLTLRAAGKTYMIFFVVIIFLGSFYLINLILAVVAMAYAEQNEATLAEDKEKEEEFQQMLEKFK 476
Nav1.5 357 DSFAWAFLALFRLMTQDCWERLYQQTLRSAGKIYMIFFMLVIFLGSFYLVNLILAVVAMAYEEQNQATIAETEEKEKRFQEAMEMLK 442
Nav1.6 354 DTFSWAFLALFRLMTQDYWENLYQLTLRAAGKTYMIFFVLVIFVGSFYLVNLILAVVAMAYEEQNQATLEEAEQKEAEFKAMLEQLK 440
Nav1.8 340 DSFAWAFLSLFRLMTQDSWERLYQQTLRTSGKIYMIFFVLVIFLGSFYLVNLILAVVTMAYEEQNQATTDEIEAKEKKFQEALEMLR 326
Nav1.9 345 DNFGWSFLAMFRLMTQDSWEKLYQQTLRTTGLYSVFFFIVVIFLGSFYLINLTLAVVTMAYEEQNKNVAAEIEAKEKMFQEAQQLLK 429
Nav1.7 905 LPRWHMNDFFHSFLIVFRVLCGEWIETMWDCMEVA--GQAMCLIVYMMVMVIGNLVVLNLFLALLLSSFSSDNLTA-IEEDPDANNL 988
Nav1.1 929 LPRWHMNDFFHSFLIVFRVLCGEWIETMWDCMEVA--GQAMCLTVFMMVMVIGNLVVLNLFLALLLSSFSADNLAA-TDDDNEMNNL 1012
Nav1.2 920 LPRWHMHDFFHSFLIVFRVLCGEWIETMWDCMEVA--GQTMCLTVFMMVMVIGNLVVLNLFLALLLSSFSSDNLAA-TDDDNEMNNL 1003
Nav1.3 921 LPRWHMNDFFHSFLIVFRVLCGEWIETMWDCMEVA--GQTMCLIVFMLVMVIGNLVVLNLFLALLLSSFSSDNLAA-TDDDNEMNNL 1004
Nav1.4 739 LPRWHMHDFFHSFLIVFRILCGEWIETMWDCMEVA--GQAMCLTVFLMVMVIGNLVVLNLFLALLLSSFSADSLAA-SDEDGEMNNL 922
Nav1.5 879 LPRWHMMDFFHAFLIIFRILCGEWIETMWDCMEVS--GQSLCLLVFLLVMVIGNLVVLNLFLALLLSSFSADNLTA-PDEDREMNNL 959
Nav1.6 914 LPRWHMHDFFHSFLIVFRVLCGEWIETMWDCMEVA--GQAMCLIVFMMVMVIGNLVVLNLFLALLLSSFSADNLAA-TDDDGEMNNL 997
Nav1.8 827 WPRWHMHDFFHSFLIVFRILCGEWIENMWACMEVG--QKSICLILFLTVMVLGNLVVLNLFIALLLNSFSADNLTA-PEDDGEVNNL 910
Nav1.9 746 LRHWHMGDFWHSFLVVFRILCGEWIENMWECMQEANASSSLCVIVFILITVIGKLVVLNLFIALLLNSFSNEERNGNLEGEARKTKV 988
Nav1.7 1387 VNFDNVGLGYLSLLQVATFKGWTIIMYAAVDSVNVDKQPKYEYSLYMYIYFVVFIIFGSFFTLNLFIGVIIDNFNQQKKKLGGQDIF 1473
Nav1.1 1413 VNFDNVGFGYLSLLQVATFKGWMDIMYAAVDSRNVELQPKYEESLYMYLYFVIFIIFGSFFTLNLFIGVIIDNFNQQKKKFGGQDIF 1499
Nav1.2 1403 VNFDNVGLGYLSLLQVATFKGWMDIMYAAVDSRNVELQPKYEDNLYMYLYFVIFIIFGSFFTLNLFIGVIIDNFNQQKKKFGGQDIF 1489
Nav1.3 1398 VNFDNVGAGYLALLQVATFKGWMDIMYAAVDSRDVKLQPVYEENLYMYLYFVIFIIFGSFFTLNLFIGVIIDNFNQQKKKFGGQDIF 1484
Nav1.4 1225 VNYDNVGLGYLSLLQVATFKGWMDIMYAAVDSREKEEQPQYEVNLYMYLYFVIFIIFGSFFTLNLFIGVIIDNFNQQKKKLGGKDIF 1311
Nav1.5 1402 VNFDNVGAGYLALLQVATFKGWMDIMYAAVDSRGYEEQPQWEYNLYMYIYFVIFIIFGSFFTLNLFIGVIIDNFNQQKKKLGGQDIF 1486
Nav1.6 1390 INFDNVGAGYLALLQVATFKGWMDIMYAAVDSRKPDEQPKYEDNIYMYIYFVIFIIFGSFFTLNLFIGVIIDNFNQQKKKFGGQDIF 1476
Nav1.8 1348 VNFDNVAMGYLALLQVATFKGWMDIMYAAVDSREVNMQPKWEDNVYMYLYFVIFIIFGGFFTLNLFVGVIIDNFNQQKKKLGGQDIF 1434
Nav1.9 1238 VNFDNVGNAYLALLQVATFKGWMDIIYAAVDSTEKEQQPEFESNSLGYIYFVVFIIFGSFFTLNLFIGVIIDNFNQQQKKLGGQDIF 1324
Nav1.7 1685 GNSMICLFQITTSAGWDGLLAPILNSKPPDCDPKKVHPGSSVEGDCGNPSVGIFYFVSYIIISFLVVVNMYIAVILENFSVATEEST 1771
Nav1.1 1710 GNSMICLFQITTSAGWDGLLAPILNSKPPDCDPNKVNPGSSVKGDCGNPSVGIFFFVSYIIISFLVVVNMYIAVILENFSVATEESA 1797
Nav1.2 1700 GNSMICLFQITTSAGWDGLLAPILNSGPPDCDPDKDHPGSSVKGDCGNPSVGIFFFVSYIIISFLVVVNMYIAVILENFSVATEESA 1787
Nav1.3 1695 GNSMICLFQITTSAGWDGLLAPILNSAPPDCDPDTIHPGSSVKGDCGNPSVGIFFFVSYIIISFLVVVNMYIAVILENFSVATEESA 1782
Nav1.4 1522 GNSIICLFEITTSAGWDGLLNPILNSGPPDCDPNLENPGTSVKGDCGNPSIGICFFCSYIIISFLIVVNMYIAIILENFNVATEESS 1609
Nav1.5 1700 ANSMLCLFQITTSAGWDGLLSPILNTGPPYCDPTLPNS-NGSRGDCGSPAVGILFFTTYIIISFLIVVNMYIAIILENFSVATEEST 1783
Nav1.6 1691 GNSMICLFQITTSAGWDGLLLPILNR-PPDCSLDKEHPGSGFKGDCGNPSVGIFFFVSYIIISFLIVVNMYIAIILENFSVATEESA 1777
Nav1.8 1647 ANSMLCLFQITTSAGWDGLLSPILNTGPPYCDPNLPNS-NGTRGDCGSPAVGIIFFTTYIIISFLIVVNMYIAVILENFNVATEEST 1733
Nav1.9 1537 ASSMLCLFQISTSAGWDSLLSPMLRSK-ESCNS--------SSENCHLPGIATSYFVSYIIISFLIVVNMYIAVILENFNTATEESE 1615